


## RESEARCH ARTICLE

# Absence of R-Ras1 and R-Ras2 causes mitochondrial alterations that trigger axonal degeneration in a hypomyelinating disease model

Berta Alcover-Sanchez<sup>1</sup> | Gonzalo Garcia-Martin<sup>1</sup> | Juan Escudero-Ramirez<sup>1</sup> |  
 Carolina Gonzalez-Riano<sup>2</sup> | Paz Lorenzo<sup>2</sup> | Alfredo Gimenez-Cassina<sup>1</sup> |  
 Laura Formentini<sup>1</sup> | Pedro de la Villa-Polo<sup>3,4</sup> | Marta P. Pereira<sup>1</sup> |  
 Francisco Wandosell<sup>1</sup> | Beatriz Cubelos<sup>1</sup> 

<sup>1</sup>Departamento de Biología Molecular and Centro Biología Molecular "Severo Ochoa", Universidad Autónoma de Madrid - Consejo Superior de Investigaciones Científicas, Madrid, Spain

<sup>2</sup>CEMBIO (Centre for Metabolomics and Bioanalysis), Facultad de Farmacia, Universidad San Pablo-CEU, CEU Universities, Madrid, Spain

<sup>3</sup>Departamento de Biología de Sistemas, Universidad de Alcalá, Madrid, Spain

<sup>4</sup>Grupo de Neurofisiología Visual, Instituto Ramón y Cajal de Investigación Sanitaria (IRYCIS), Madrid, Spain

## Correspondence

Beatriz Cubelos, Departamento de Biología Molecular, Centro de Biología Molecular Severo Ochoa, Nicolás Cabrera 1, Universidad Autónoma de Madrid, 28049 Madrid, Spain.  
 Email: bcubelos@cbm.csic.es

## Funding information

Spanish Ministry of Economy and Competitiveness, Grant/Award Numbers: RTI2018-096303B-C31, RTI2018-096303B-C33, RTI2018-095166B-I00; European Regional Development Fund, Grant/Award Numbers: FIS/PI 18-00754, RD16/0008/0020

## Abstract

Fast synaptic transmission in vertebrates is critically dependent on myelin for insulation and metabolic support. Myelin is produced by oligodendrocytes (OLs) that maintain multilayered membrane compartments that wrap around axonal fibers. Alterations in myelination can therefore lead to severe pathologies such as multiple sclerosis. Given that hypomyelination disorders have complex etiologies, reproducing clinical symptoms of myelin diseases from a neurological perspective in animal models has been difficult. We recently reported that *R-Ras1*<sup>-/-</sup> and/or *R-Ras2*<sup>-/-</sup> mice, which lack GTPases essential for OL survival and differentiation processes, present different degrees of hypomyelination in the central nervous system with a compounded hypomyelination in double knockout (*DKO*) mice. Here, we discovered that the loss of R-Ras1 and/or R-Ras2 function is associated with aberrant myelinated axons with increased numbers of mitochondria, and a disrupted mitochondrial respiration that leads to increased reactive oxygen species levels. Consequently, aberrant myelinated axons are thinner with cytoskeletal phosphorylation patterns typical of axonal degeneration processes, characteristic of myelin diseases. Although we observed different levels of hypomyelination in a single mutant mouse, the combined loss of function in *DKO* mice lead to a compromised axonal integrity, triggering the loss of visual function. Our findings demonstrate that the loss of R-Ras function reproduces several characteristics of hypomyelinating diseases, and we therefore propose that *R-Ras1*<sup>-/-</sup> and *R-Ras2*<sup>-/-</sup> neurological models are valuable approaches for the study of these myelin pathologies.

## KEYWORDS

mitochondria, multiple sclerosis, myelin, neurodegeneration, oligodendrocyte, R-Ras



## 1 | INTRODUCTION

Myelin is critically required in the vertebrate's nervous system to enable fast and efficient synaptic transmission. In the central nervous system (CNS), oligodendrocytes (OLs) are responsible for myelination, in a complex process involving various cellular interactions.

OLs are generated from oligodendrocyte progenitor cells (OPCs), characterized by different migratory capacities, morphological complexity, gene expression pattern, and specific marker expressions (Foerster, Hill, & Franklin, 2019; Sock & Wegner, 2019). After differentiating from OPCs, mature OLs create myelin and extend the processes that wrap around axons to form compact myelin sheaths (Foster, Bujalka, & Emery, 2019; Hill & Grutzendler, 2019; Snaidero & Simons, 2017). These multilayered membrane compartments, or nodes, line up along the axon to provide metabolic support and protection from the extracellular space (Lee et al., 2012; Saab, Tzvetanova, & Nave, 2013; Simons & Nave, 2016). Between nodal compartments lies the Nodes of Ranvier, structures in which the molecular machinery responsible for electric transmission is concentrated. This organization enables fast saltatory conduction of action potentials initiated at the neuronal soma because the axonal membrane depolarization skips from node to node (Nave & Werner, 2014), a feature believed to contribute to vertebrate evolution (Timmler & Simons, 2019).

Myelin's role is so important that when it is impaired or lost, pathologies begin to appear (Lüders et al., 2019). The onset of myelin dysfunction can impact a wide range of processes; from embryonic development to chronic degenerative diseases such as multiple sclerosis (MS) (Boespflug-Tanguy, Labauge, Fogli, & Vaurs-Barriere, 2008; Suter & Scherer, 2003). At the cellular level, lack of myelin causes channels responsible for depolarization to become distributed along the axon instead of being concentrated in the Nodes of Ranvier, requiring greater number of depolarizations and increased use of ATP to fuel synaptic transmission (Craner, Hains, Lo, Black, & Waxman, 2004; Waxman, 1998). When whole-cell ATP levels are depleted, Na<sup>+</sup>/K<sup>+</sup> ATPase is then unable to restore the Na<sup>+</sup>/K<sup>+</sup> gradient after an action potential, which leads to degeneration and axonal dysfunction (Trapp & Stys, 2009; Tsutsui & Stys, 2013). To compensate for increased axonal energy demands, both the numbers and activity of mitochondria in dys-demyelinated areas increase; a well characterized feature of myelin diseases demonstrated both in humans and in numerous animal models (Andrews et al., 2006; Mutsaers & Carroll, 1998; Sathornsumetee, McGavern, Ure, & Rodriguez, 2000; Witte et al., 2009).

PI3K/Akt/mTOR and MAPK pathways are both described as intracellular regulators of myelination. Specifically, PI3K/Akt/mTOR and Erk1/2-MAPK signaling pathways regulate OL survival, migration, and differentiation (Figlia, Gerber, & Suter, 2018; Gaesser & Fyffe-Maricich, 2016; Guardiola-Diaz, Ishii, & Bansal, 2012; Ishii, Furusho, Dupree, & Bansal, 2014; Ishii, Furusho, Macklin, & Bansal, 2019; Murcia-Belmonte et al., 2016; Murcia-Belmonte, Medina-Rodríguez, Bribián, de Castro, & Esteban, 2014; Ness, Mitchell, & Wood, 2002; Romanelli, Mahajan, Fulmer, & Wood, 2009). Both Akt and MAPK pathways are also coalesce on Ras effector proteins within the

GTPase superfamily, which broadly regulates proliferation (Colicelli, 2004). We recently reported that OLs express R-Ras1 and R-Ras2, and that the absence of R-Ras1 and R-Ras2 reduces the activation of the PI3K/Akt/mTOR and MAPK signaling pathways, causing a decrease in OL differentiation and survival. Although double knock-out (DKO) mice had dramatic CNS myelination defects, mice lacking R-Ras1 or R-Ras2 differed somewhat in their hypomyelination phenotypes, suggesting that nonoverlapping mechanisms synergize to bring about more severe myelin defects (Sanz-Rodriguez et al., 2018).

In spite of these advances, our insight into how different levels of hypomyelination, caused by the loss of R-Ras1, R-Ras2, or both, affect the neuronal function, remains limited. In this work, we discovered that different degrees of hypomyelination in adult mice lead to different mitochondrial adaptations. In *R-Ras1*<sup>-/-</sup> (*R-Ras1KO*) mice, where the thickness of the axonal myelin sheath was reduced, mitochondrial complexes involved in oxidative phosphorylation (OXPHOS) were upregulated, supporting an increased oxygen consumption rate (OCR). In *R-Ras2*<sup>-/-</sup> (*R-Ras2KO*) mice, where fewer axons were myelinated, the numbers of mitochondria were increased in nonmyelinated axons. These two phenotypes were compounded in *R-Ras1*<sup>-/-</sup>;*R-Ras2*<sup>-/-</sup> (DKO) mice to cause increased reactive oxygen species (ROS) levels, axonal degeneration, and neuronal loss.

## 2 | MATERIALS AND METHODS

### 2.1 | Animals

C57BL6 mice were housed in specific pathogen-free conditions in a humidity- and temperature-controlled room, in a 12 hr light/dark cycle, receiving water and food ad libitum. All experiments were performed in male and female mice. All animal procedures were approved by the corresponding institutional ethical committee (Centro de Biología Molecular Severo Ochoa [CBMSO]) and were performed in accordance with Spanish and European guidelines. All efforts were made to minimize animal suffering.

*R-Ras1*<sup>-/-</sup> mice were generated at GenoWay (Lion, France) using the targeting construction BAL1-HR with a neomycin resistance cassette flanked by FRT sequences, inserted in Intron 1 and LoxP sites, flanking Exons 2 and 6. The construction was electroporated into embryonic stem cells derived from mouse 129Sv/Pas and selected by G418 antibiotic. Southern blot was used to verify the correct homologous recombination.

Heterozygous mice were crossed, and offspring littermates were genotyped by PCR (*R-Ras1*<sup>-/-</sup> FW: 5'-GGAGCAAGAGGAGGGAAGG AATGGG-3', *R-Ras1*<sup>-/-</sup> RV: 5'-CCTTCCAGAGGACTCAGTTCATCC-3', *R-Ras1*<sup>+/+</sup> FW: 5'-CGCTCTAGCTGAGCCTCTGT-3', *R-Ras1*<sup>+/+</sup> RV: 5'-TACAGGGTCTGTGGGGAAA-3').

*R-Ras2*<sup>-/-</sup> mice were generated at Lexicon Pharmaceuticals (TX) and were derived from embryonic stem cell clone OST361011 with insertion of retroviral VICTR37 in the middle of Intron 1 of *R-Ras2*. Heterozygous mice were crossed and offspring littermates were genotyped by PCR (primer 1, 5'-TGAAACAGGATCATGTTGTGGAG-3'; primer 2, 5'-

CAGGAGGAGTCCAAGAAGAC-3'; primer 3, 5'-ATAAACCTCTTGACGTTGCATC-3') (Delgado et al., 2009). *R-Ras2<sup>+/+</sup>* and *R-Ras2<sup>-/-</sup>* transgenic mice were obtained by crossing heterozygous mice.

*R-Ras1<sup>-/-</sup>* and *R-Ras2<sup>-/-</sup>* mice were kindly provided by Prof B. Alarcón (CBMSO, Spain). DKO *R-Ras1<sup>-/-</sup>;R-Ras2<sup>-/-</sup>* mice were generated by backcrossing individual lines *R-Ras1<sup>-/-</sup>* and *R-Ras2<sup>-/-</sup>*. Animals were maintained in a C57BL6J background. We used either male or female mice to perform the experiments. We defined the newborn as postnatal 0 (P0).

## 2.2 | Western blotting

Tissue samples (optic nerve, cerebral cortex, and the total brain of animals from P0 to adults [P90]) were dissected, resuspended in lysis buffer (50 mM Tris pH 8.0, 150 mM NaCl, 1% NP40, 2 mM EDTA, 0.1% SDS, 0.5% deoxycholate, and protease inhibition mixture; Roche 11697498001), and phenylmethane sulfonyl fluoride. Lysates were denatured by boiling them for 5 min in protein loading buffer (50 mM Tris-HCl pH 6.8, 2% SDS, 10% glycerol, 1%  $\beta$ -mercaptoethanol [BME], 12.5 mM EDTA, and 0.02% bromophenol blue) and resolved in 10–12% SDS gels in the presence of BME. Gels were run at constant current starting at 90 or 100 V. After electrophoresis, samples were transferred by electroblotting onto a polyvinylidene difluoride (PVDF) membrane in a semidry electroblotting system (Transblot-turbo, Bio Rad Laboratories, Hercules, CA) at 1.2 mA/cm<sup>2</sup> for 35–40 min. Nonspecific protein binding was blocked by incubating the membrane with 5% nonfat milk in TBS-Tween-20 for 1 hr at room temperature. Membranes were incubated overnight with the pertinent primary antibodies in the blocking buffer: mouse anti-amyloid precursor protein (APP) 1:1,000 (Millipore catalog#MAB348, RRID:AB\_94882), mouse anti-ATP synthase (subunit  $\alpha$ ) 1:1,000 (Invitrogen catalog# 459240), mouse anti-UQCRC2 (ubiquinol-cytochrome c reductase complex) 1:3,000 (Thermo Fisher Scientific catalog# PA5-30204), and mouse anti-CoxIV (cytochrome oxidase subunit IV) 1:1,000 (Molecular Probes catalog# A-21348). Other antibodies used were mouse anti-GAPDH (G9) 1:1,000 (Santa Cruz Biotechnology catalog# sc-365062, RRID:AB\_10847862), mouse anti-MBP (aa67-74) 1:200 (Bio-Rad/AbD Serotec catalog# MCA685S, RRID:AB\_325009), and mouse anti-Tau 1 1:1,000 that was kindly provided by Prof J. Ávila (CBMSO, Madrid). After washing, blots were incubated for 1 hr with appropriated peroxidase-conjugated secondary antibodies (Thermo Fisher Scientific). Labeled proteins were detected with the Chemiluminescence Reagent ECL (GE Healthcare).

## 2.3 | Oxyblot (OxyBlot protein oxidation detection kit)

OxyBlot assay was performed according to the manufacturer's specifications (Sigma-Aldrich catalog# S7150). It consists of the detection of the carbonyl groups that are introduced into the amino acid side chain after oxidative modification of proteins previously derivatized to 2,4-dinitrophenyl-hydrazone (DNP-hydrazone). Then DNP-

derivatized proteins were resolved in 12% SDS-gel samples and transferred by electroblotting onto a PVDF membrane (previously activated in EtOH 95%) in a semidry electroblotting system (Transblot-turbo, Bio Rad Laboratories) at 1.2 mA/cm<sup>2</sup> for 35–40 min. Nonspecific protein binding was blocked by incubating the membrane with 5% nonfat milk in TBS-Tween-20 for 1 hr at room temperature. Then the membranes were exposed to a primary rabbit anti-DNPH protein antibody 1:100 for 1 hr, and then to a secondary goat anti-rabbit IgG (HRP-conjugated) antibody 1:300 for 1 hr at room temperature (both antibodies were diluted in TBS-Tween-20). After incubations, the membranes were washed gently with TBS-Tween-20. Finally, the detection was performed with Chemiluminescence Reagent ECL (GE Healthcare).

## 2.4 | Immunohistochemistry

Animals were anesthetized (ketamine/xylazine) and perfused transcardially with 0.1 M phosphate-buffered saline (PBS; pH 7.4) followed by 4% paraformaldehyde in PBS. Perfused tissues were removed and postfixed in 4% paraformaldehyde at 4°C overnight. Then they were cryoprotected in 30% sucrose in PBS and embedded and frozen in a 7.5% gelatin in 15% sucrose solution. Then they were sectioned on a cryostat to produce 20  $\mu$ m cryosections on Superfrost Plus microscope slides (Thermo Fisher Scientific). Sections were blocked for 1 hr at room temperature with 10% fetal bovine serum in PBS containing 0.5% Triton-X 100 (blocking solution) and then incubated overnight at 4°C with the primary antibodies: mouse anti-APP 1:500 (Millipore catalog#MAB348, RRID:AB\_94882), rabbit anti-glial fibrillary acidic protein (GFAP) 1:1,000 (Dako catalog# Z0334, RRID:AB\_10013382), rabbit anti-Iba1 1:500 (Wako catalog# 019-19741, RRID:AB\_839504), rabbit anti-cleaved caspase 3 (Asp 175) 1:500 (Cell Signaling catalog# 9661, RRID:AB\_2341188), mouse anti-SMI-32 1:1,000 (Biolegend catalog# 801701, RRID:AB\_2564642), or mouse anti-polysialylated-neural cell adhesion molecule (PSA-NCAM) 1:50 (Miltenyi Biotec 130-117-394, RRID:AB\_2727931) diluted in blocking solution. After three washes, fluorescent-tagged secondary antibodies (Alexa-488 or Alexa-647) were applied for 1 hr at room temperature, and sections were counterstained with DAPI (Sigma-Aldrich catalog# 32670) and mounted in Aqua-polymount mounting medium (Polyscience catalog# 18606).

## 2.5 | Confocal microscopy

Fluorescence images were obtained using a confocal multispectral Leica TCS SP5 system (Leica Microsystems) controlled by Las AF v 2.7 software (Leica). Image acquisition was performed sequentially using a 40 $\times$ /1.4NA oil immersion objectives and appropriate fluorochrome excitation lines (405, 488, and 647 nm for DAPI, Alexa-488, and Alexa-647, respectively). Mean intensity was quantified using Fiji/ImageJ software.



## 2.6 | Electron microscopy

Mutant and littermate control mice were anesthetized as indicated above, intracardially perfused with 4% paraformaldehyde and 2.5% glutaraldehyde in 0.1 M PBS and treated in the same fixative overnight. Optic nerves were then removed after several washes in PBS and the sections were postfixed with 1% osmium tetroxide in double-distilled water and 1% potassium ferrocyanide 1 hr at 4°C. After three washes with double-distilled water, they were treated with 0.15% of tannic acid in 0.1 M PBS, pH 7.4, and block-stained with 2% uranyl acetate in distilled water for 1 hr room temperature, in darkness. Sections were then washed three times with double-distilled water and dehydrated in an ascending series of ethanol dilutions of up to 100% at 4°C. The following infiltration was made with propylene oxide:EtOH (1:1; vol:vol) for 5 min, propylene oxide three times at 15 min each, propylene oxide:Epon (1:1) (epoxy resin TAAB 812, TAAB Laboratories) for 45 min, and 100% Epon 1 hr and Epon 100% overnight. Encapsulation was made in flat molds where optic nerves were correctly orientated and then polymerized 48 hr at 60°C. The optic nerve was cut in 70–80 nm sections on an ultramicrotome (Leica Ultracut UCT) with a diamond blade (Diatome) and collected on Cu-Pd boutonniere grids covered by Formvar. Staining of ultrathin sections was performed by drops of 2% aqueous uranyl acetate for 7 min, followed by Reynolds's lead citrate for 2 min. Ultrastructural analyses were performed with a JEM-1010 electron microscope (JEOL).

In cross sections, 12 photographs per mice were taken along the section covering the whole diameter of the optic nerve, using a CMOS 4 K × 4 K, F416 de TVIPS camera (Gauting). Images were taken at 12,000× magnification. A total area of 302.58 μm<sup>2</sup> was accounted for per genotype. From these pictures, six in perfect condition that matched the mutants and controls, were used to identify astrogliosis processes.

In longitudinal sections, 10 photographs per mice were taken along the section covering the whole length of the optic nerve. For the mitochondrial quantification, images were taken at 6,000× magnification and a total area of 2,017.2 μm<sup>2</sup> was accounted for per genotype. Mitochondria were identified as cylindrical double-membrane structures with interior crista membranes and classified between myelinated and nonmyelinated axons. For the mitochondrial area, 394 axons in controls, 376 axons in *R-Ras1KO*, 469 axons in *R-Ras2KO*, and 498 axons in *DKO* were analyzed.

For the axonal dystrophy elements quantification, 10 photographs per genotype were analyzed in transversal sections of the optic nerve. Images were taken at 3,000× magnification and a total area of 2,680 μm<sup>2</sup> was accounted for per genotype. Axonal dystrophy elements were identified as swollen axons containing autophagosomes, autophagolysosomes, and multivesicular bodies (MVBs) structures in the axons.

Three animals per genotype were analyzed. Identical results were obtained independently, four times, by different investigators.

## 2.7 | Brain mitochondrial isolation

Fresh brains from the wild-type (WT), and P90 and P0 transgenic mice were minced and homogenized in a glass-glass homogenizer in buffer A (320 mM sucrose, 1 mM EDTA, and 10 mM Tris-HCl, and pH 7.4). Brain mitochondria were obtained by centrifugation. Briefly, unbroken cells and tissue were removed by centrifugation at 1,000g for 5 min at 4°C. Synaptosomes present in the supernatant were permeabilized with 100 μM digitonine and mitochondria were obtained by supernatant centrifugation at 11,000g for 15 min at 4°C. Mitochondria were resuspended in Buffer B (0.25 mM sucrose, 10 mM Tris-HCl, and pH 7.4, 0.1% [m/v] BSA).

## 2.8 | Oxygen consumption rate

Mitochondrial OCR in isolated mitochondria (200 μg protein) was determined with a Clark-type electrode. After proper calibration, mitochondria were placed in the chamber with continuous stirring in respiration buffer (225 mM sucrose, 5 mM MgCl<sub>2</sub>, 10 mM KCl, 10 mM phosphate buffer, 1 mM EGTA, 0.05% BSA and 10 mM Tris-HCl, pH 7.4). Four different compounds were added to test the mitochondrial function and describe changes in respiration states in mutant mice compared to controls. Then, 10 μM glutamate plus malate was used as respiratory substrates for electron donation to mitochondrial Complex I. The basal respiration state was measured prior to the addition of ADP (Pseudo state IV) and was controlled only by proton leak and substrate oxidation. Addition of 0.5 mM ADP under saturated substrate and oxygen (State III) allowed for the stimulation of the ATP synthase to test the OXPHOS activity. State III activity was ended by the addition of 5 μM oligomycin (O), an inhibitor of ATP synthase which made it possible to obtain State IV measurements. In this state, respiration was highly dependent on proton leak. By injection of 5 μM FCCP proton flux was restored, allowing for the measurements of the maximum respiratory capacity independently of ATP synthase activity (Uncoupled State III). Finally, 1 μM antimycin A (Ant A) was used to inhibit all respiration and test the residual oxygen consumption.

## 2.9 | Extracellular flux analysis (“Seahorse assay”)

Seahorse assay on neurons and glial cells was performed as described previously (Katsu-Jiménez & Giménez-Cassina, 2019). OCR, ATP-coupled respiration, and maximal respiration capacity were determined in real time using XF24 extracellular flux analyzer (Seahorse Bioscience-Agilent, Santa Clara, CA). Purified and independent neurons and OLs cultures were seeded at  $1.5 \times 10^5$  or  $4 \times 10^4$  cells per well, respectively, in specific growth medium and

then analyzed using the Seahorse XF24 extracellular flux analyzer. One hour prior to the experiment, culture medium was replaced by assay medium consisting of bicarbonate-free DMEM supplemented with 5 mM glucose and 1 mM sodium pyruvate. After the baseline measurement, the following sequential injections were made to determine ATP-coupled respiration and maximal respiratory capacity: 1  $\mu$ M oligomycin, 0.5  $\mu$ M carbonyl cyanide-4 (trifluoromethoxy) phenylhydrazone (FCCP), and 4  $\mu$ M rotenone/antimycin A.

## 2.10 | Metabolomics

The metabolomics assay was performed at CEMBIO (Madrid, Spain), as described previously (Gonzalez-Riano et al., 2018). Briefly, the gas chromatography–mass spectrometry (GC–MS) analysis was developed with optic nerve samples from the controls, single, and double-mutant mice. Optic nerves were dissected from P90 mice after cervical dislocation. Samples were then kept at  $-80^{\circ}\text{C}$  immediately, until the day of the analysis. First, 100  $\mu$ l of cold methanol ( $-20^{\circ}\text{C}$ ) containing 25 ppm of pentadecanoic acid used as an internal standard (IS) was added to each sample. Subsequently, samples were homogenized using a 2 mm particle size glass beads from TissueLyser LT homogenizer (Qiagen, Germany), centrifuged at 13,000 g at  $4^{\circ}\text{C}$  for 10 min, and 80  $\mu$ l of the supernatant from each sample was transferred to the GC–MS vial. Supernatants were evaporated until dryness using a SpeedVac Concentrator System. Later, samples were chemically derivatized with two reactions, methoxymation and then silylation, for the GC–MS analysis. Before the analysis, 100  $\mu$ l of heptane containing 10 ppm of methyl stearate C18:0 as a second IS was added. Finally, 2  $\mu$ l of derivatized sample was injected in a split mode (1:10) into a GC instrument 7890A (Agilent Technologies, Germany) coupled to an inert mass spectrometer with the Triple-Axis detector 5975C (Agilent Technologies). The quality and the robustness of the analytical run was evaluated using quality control samples prepared by pooling equal volumes of homogenate from each sample. Raw data files were imported into Agilent Mass Hunter Unknown Analysis Tool 7.0 for the peak detection, deconvolution, and metabolite identification. The software executed a search against two targeted libraries to obtain a chemical identity for the compounds: Fiehn version 2013 and the CEMBIO internal spectrum library, always comparing both the retention time and the spectra extracted during deconvolution against each compound included in the library. A third commercial library—NIST (National Institute of Standards and Technology, library 2.2 version 2017)—was used for unknown identification. Those metabolites with a spectrum score of  $\geq 80\%$  and a concordant retention index based on the *n*-alkane scale were tentatively identified according to this library. Data were filtered by the signal coefficient variation in QC, considering acceptable values below 30%. Finally, altered metabolic pathways were analyzed using MetaBoAnalyst 4.0 (Chong, Wishart, & Xia, 2019).

## 2.11 | Optomotor response

Optomotor test was performed as described previously (Prusky, Alam, Beekman, & Douglas, 2004). This test was proposed as a test of adequate animal behavior to evaluate the functional state of the retina's visual function in mice that suffer from retinal degenerations. Experimental animals respond to visualized rotating vertical bars by characteristic reflex movement of their head in the same direction to the bars' rotation. Contrast sensitivity is actually used as an evidence of visual discrimination (Umino, Solessio, & Barlow, 2008). A homemade optomotor device was built based on previous study (Prusky et al., 2004). Mice were placed at the center of a square array of computer monitors that displayed stimulus gratings. Mice were monitored by the use of infrared television camera placed on top of the testing chamber. The visual test consisted of vertical black/white bars (gratings) of distinct spatial frequencies (0.011–0.355 cycles/ $^{\circ}$ ) moving through the screens. Contrast sensitivity was calculated as the inverse of contrast threshold between white and black bars. Maximum contrast (value = 1) was measured for white screen luminance of 122.70 cd/m<sup>2</sup> and black screen luminance of 0.25 cd/m<sup>2</sup>. The Vision Egg tool was used for the light stimulation. The test started with the easiest stimulus for the mice, with a spatial frequency of 0.088 cycles/ $^{\circ}$ , a temporal frequency of 0.88 Hz, and a normalized contrast of 1.

## 2.12 | Paw-print test

This test allows for the detection of motor impairment (Maggipinto et al., 2017). Mice were habituated to the test room for 1 hr before administration of the tests that were carried out during the light cycle. Mice paws in both forelimbs and hindlimbs were painted and the mice then walked on a 40 cm  $\times$  12 cm white piece of paper. Several gait parameters were measured using ImageJ software: stride length (the distance between two same-sided forelimbs or two same-sided hindlimbs), base width (side-to-side distance between the line of the two paws of fore or hindlimbs), paw placement (calculated as the angle between the long axes of the paw and the centerline of the mouse), and regularity index (percentage of correct step sequences over the total number of step cycle).

## 2.13 | Statistical analysis

Quantitative data are shown as the mean  $\pm$  SD. The experimental groups were compared using a two-tailed Student's *t* test. Statistical numeric data are provided in the figure legends. (\*) means  $p < .05$ ; (\*\*) means  $p < .01$ ; (\*\*\*) means  $p < .001$ . For metabolomics statistical analysis, we used Benjamini and Hochberg and Mann–Whitney U tests. An alpha level of .05 was considered significant. Outliers were identified using boxplots. These outliers were discarded as being outside





the median trend. For the optomotor response statistical analysis, we used the two-way analysis of variance test and Bonferroni post tests.

### 3 | RESULTS

#### 3.1 | Absence of R-Ras2 leads to increased numbers of axonal mitochondria

We recently reported that the loss of R-Ras1 and/or R-Ras2 decreases the myelin levels in adult mice, which is reflected as thinner myelin sheaths, reduced numbers of OLs, and less wrapping of the myelinated axons (Sanz-Rodriguez et al., 2018). Here, we set out to investigate the metabolic adaptation and neuronal dysfunction resulting from the R-Ras loss of function, as mechanisms mimicking aspects of myelinating disorders. We first set out to perform additional electron microscopy analysis of optic nerve longitudinal sections to quantify the relationships between myelination defects, mitochondrial phenotype, and R-Ras genotypes. Consistent with our prior data, visual inspection of sections from *R-Ras1KO* mice showed thinner myelin layers whereas sections from *R-Ras2KO* mice had fewer myelinated axons relative to sections from WT mice. Consolidating these phenotypes, sections from *DKO* mice showed an overall more severe myelin phenotype (Figure 1a). We found that axonal numbers of mitochondria were increased in *R-Ras2KO* and *DKO* mice. To determine whether there is a difference between increase in mitochondrial density and lack of axonal myelination, we next quantified the number of mitochondria present in myelinated and nonmyelinated axons. We found that myelinated axons in mice across controls and all *R-Ras* genotypes contained roughly equal numbers of mitochondria (mitochondria per myelinated axon WT:  $1.31 \pm 0.15$ ; *R-Ras1KO*:  $1.26 \pm 0.10$ ; *R-Ras2KO*:  $1.48 \pm 0.36$ ; and *DKO* mice:  $2.41 \pm 0.94$ ) (Figure 1b). In contrast, axons lacking myelin sheath contained significantly more mitochondria in both *R-Ras2KO* and *DKO* mice (mitochondria per nonmyelinated axons:  $0.61 \pm 0.18$ ,  $p < .05$  and  $0.75 \pm 0.23$ ,  $p < .05$ ) relative to WT and *R-Ras1KO* (mitochondria per nonmyelinated axon:  $0.22 \pm 0.08$  and  $0.16 \pm 0.08$ ) (Figure 1c). This ratio revealed that a complete lack of myelin increases the number of mitochondria in *R-Ras2KO* and *DKO* mice whereas the normalized mitochondrial number count was comparable in WT and *R-Ras1KO* mice. To determine whether the absence of R-Ras1 and/or R-Ras2 altered the mitochondrial size, we measured the mitochondrial area. Quantification revealed an increase in the average mitochondrial area in nonmyelinated axons in *R-Ras1KO* mice ( $0.21 \pm 0.06 \mu\text{m}^2$ ,  $p < .05$ ), *R-Ras2KO* and *DKO* mice showed a decrease in average mitochondrial area in nonmyelinated axons (for *R-Ras2KO*:  $0.091 \pm 0.05 \mu\text{m}^2$ ,  $p < .05$  and for *DKO*:  $0.083 \pm 0.03 \mu\text{m}^2$ ,  $p < .001$ ) relative to the controls ( $0.14 \pm 0.08 \mu\text{m}^2$ ) (Figure 1e). No alterations in mitochondria size were observed in myelinated axons (Figure 1d). These data indicate that a lack of the myelin sheath leads to a mitochondrial adaptation, reflected as size alterations and an increase in the numbers of axonal mitochondria,

whereas a mere decrease in the thickness of the myelin sheath surrounding the axons appears to be insufficient to impact on the number of the mitochondria (Figure 1f).

#### 3.2 | Absence of R-Ras1 increases the protein levels of mitochondrial complexes

We next asked whether R-Ras loss of function genotypes resulted in changes in mitochondrial activity. To answer this question, we quantified whether the levels of proteins executing mitochondrial OXPHOS in the optic nerve homogenates in adult mutant mice and WT controls. In OXPHOS, a group of complexes in the inner mitochondrial membrane create ATP by coordinating serial redox reactions to free up the energy captured in the double oxygen bond. With the western blot analysis, we found that abundance of Complex III (UQCRC2; cytochrome c reductase), Complex IV (COX IV; cytochrome c oxidase), and/or complex V (ATP synthase) subunits were increased in *R-Ras1KO* and *DKO* mice (Figure 2a). We did not detect any significant differences between *R-Ras2KO* homogenates and controls. The fold-change in protein level values for the different mitochondrial complexes relative to controls were as follows: ATP synthase: *R-Ras1KO* =  $1.97 \pm 0.09$  ( $p < .001$ ); *R-Ras2KO* =  $1.37 \pm 0.76$ ; *DKO* =  $2.08 \pm 0.84$  ( $p < .05$ ). COX IV: *R-Ras1KO* =  $2.45 \pm 0.45$  ( $p < .001$ ); *R-Ras2KO* =  $1.13 \pm 0.36$ ; *DKO* =  $2.67 \pm 0.21$  ( $p < .001$ ). UQCRC2: *R-Ras1KO* =  $0.91 \pm 0.29$ ; *R-Ras2KO* =  $0.93 \pm 0.70$ ; *DKO* =  $3.40 \pm 0.92$  ( $p < .001$ ) (Figure 2a). To ascertain if the observed increases in protein levels of OXPHOS components were specific to myelin-dependent tracts, such as the optic nerve, we repeated the western blot analysis in homogenates of myelin less-dependent tracts. For ATP synthase, these were: *R-Ras1KO* =  $1.22 \pm 0.02$  increase; *R-Ras2KO* =  $1.18 \pm 0.15$ ; *DKO* =  $1.24 \pm 0.36$ . For COXIV: *R-Ras1KO* =  $0.91 \pm 0.04$ ; *R-Ras2KO* =  $0.91 \pm 0.02$ ; *DKO* =  $0.87 \pm 0.21$ . For UQCRC2: *R-Ras1KO* =  $1.02 \pm 0.07$ ; *R-Ras2KO* =  $1.05 \pm 0.22$ ; *DKO* =  $1.13 \pm 0.34$  (Figure 2b). We found no differences in the protein levels of ATP synthase, UQCRC2, or COXIV in mutant mice in less-dependent myelin tissues (Figure 2b).

Taken together, these data show that the loss of R-Ras1 leads to increased levels of mitochondrial complexes (UQCRC2, COXIV, and ATP synthase) only, in myelin-dependent tracts, without causing alterations in weakly myelinated brain regions.

#### 3.3 | Loss of R-Ras1 increases oxygen consumption in the adult brain

To understand whether R-Ras1 and R-Ras2 loss leads to functional changes in mitochondrial activity, we measured OCR in purified mitochondria, isolated from adult brains using a Clark-type electrode (Figure 3a). We did not observe quantifiable changes in State IV, Pseudo State IV, uncoupled-State III, and inhibited respiration across genotypes (Figure 3a,c). However, we found that ADP-stimulated State III respiration (expressed as nmol O/min/mg protein) was

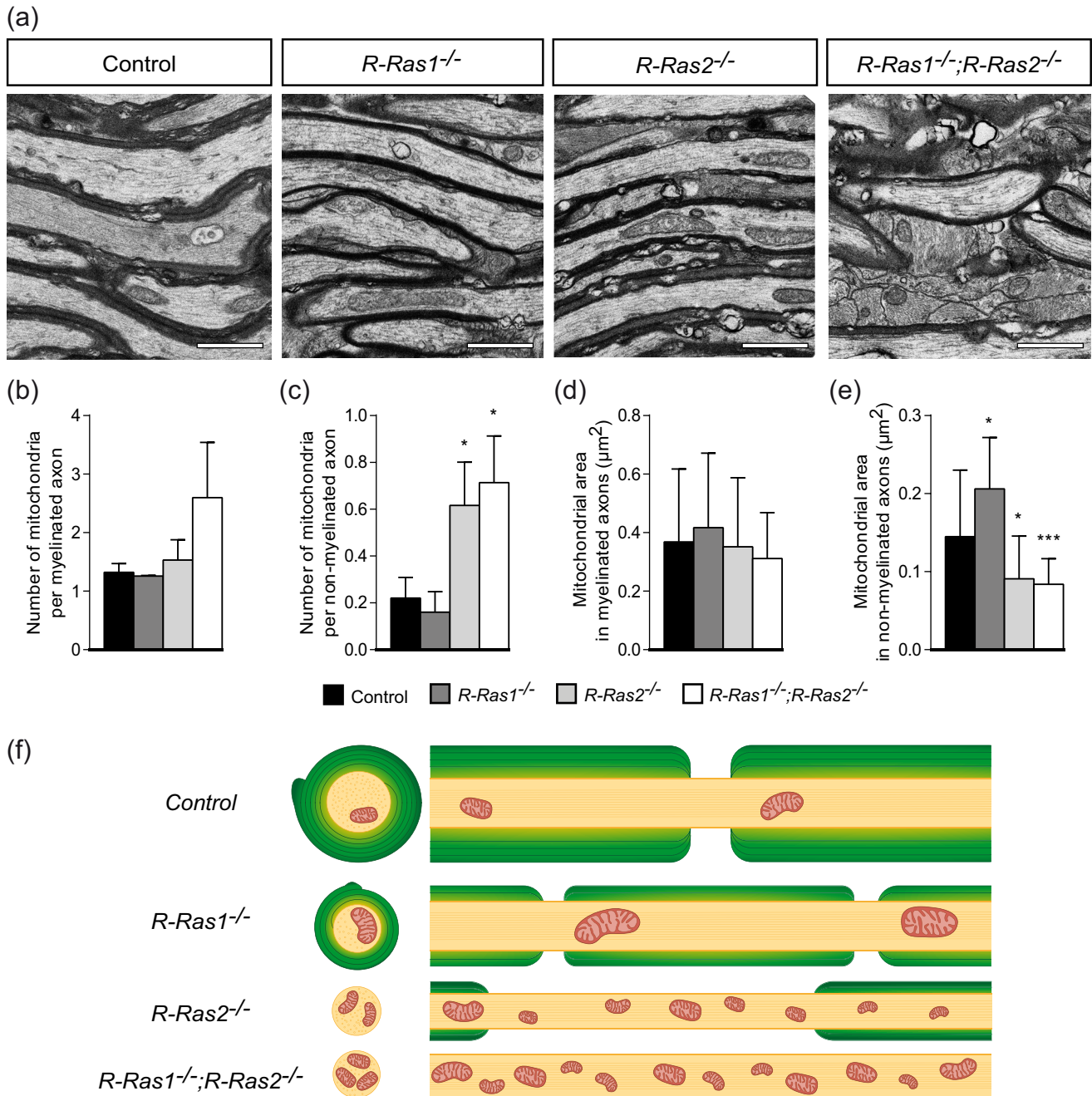


**FIGURE 1** Loss of *R-Ras2* affects axonal myelination of the optic nerves causing an increase in the mitochondria in nonmyelinated axons. (a) Electron microscopy of the longitudinal sections of the optic nerve of adult (P90) control, *R-Ras1*<sup>-/-</sup>, *R-Ras2*<sup>-/-</sup>, and *R-Ras1*<sup>-/-</sup>; *R-Ras2*<sup>-/-</sup> double knockout mice. There was a significant increase in nonmyelinated axons in the absence of *R-Ras2* in single and double-mutants compared to controls. (b) The number of mitochondria per myelinated axon in the optic nerve of adult mice (P90) revealed no differences between single and double-mutants relative to controls. (c) The number of mitochondria per nonmyelinated axon present in the optic nerve of adult mice (P90) showed significant differences between *R-Ras2*<sup>-/-</sup> ( $*p < .05$ ) and the double-mutant mice ( $*p < .05$ ). (d) The average number of mitochondria area per myelinated axon present in the optic nerve of adult mice (P90) revealed no differences between single and double-mutants relative to controls. (e) The average number of mitochondria area per nonmyelinated axon present in the optic nerve of adult mice (P90) showed significant differences in *R-Ras1*<sup>-/-</sup> ( $*p < .05$ ), *R-Ras2*<sup>-/-</sup> ( $*p < .05$ ), and the double-mutant mice ( $***p < .001$ ). (f) Schematic representation of the mitochondria alteration in the longitudinal and transverse sections of the axons with myelin deficits in single and double mutant mice relative to controls. ( $n = 3$  mice per genotype). Bar graph represents the mean  $\pm$  SD of controls. Two-tailed Student's *t* test was used for the statistical analysis. Scale bar, 1  $\mu$ m. SD, standard deviation [Color figure can be viewed at [wileyonlinelibrary.com](http://wileyonlinelibrary.com)]

significantly elevated in *R-Ras1KO* ( $38.6 \pm 7.4$ ,  $p < .05$ ) and in *DKO* mitochondria ( $31.3 \pm 3.1$ ,  $p < .05$ ) relative to WT and *R-Ras2KO* ( $18.3 \pm 3.4$  and  $14.6 \pm 2.5$ ) (Figure 3c).

We next asked whether the increase in OXPHOS activity in *R-Ras1KO* and *DKO* mice was dependent on the presence of myelin. To this end, we analyzed the OCR in a nonmyelinated tissue (Figure 3b, d), specifically, in mitochondria isolated from neonatal P0 mouse brain but we did not find any alterations in mitochondrial function in neonatal *R-Ras* mutant mice. State III respiration (nmol O/min/mg protein) was:  $23.4 \pm 1.4$  for WT;  $23.9 \pm 1.0$  for *R-Ras1KO*;  $20.6 \pm 6$  for *R-Ras2KO*; and  $18.8 \pm 3.9$  for *DKO* mice (Figure 3d). Taken together, these data show that myelin deficiency in adult mice resulting from

the loss of *R-Ras1* leads to a compensatory increase in mitochondrial activity, with no observed changes in mitochondrial respiration in nonmyelin-dependent tissues.

### 3.4 | Absence of *R-Ras1* and/or *R-Ras2* does not affect mitochondrial activity in OLs and isolated neurons

To assess possible cell-intrinsic mitochondrial alterations in *Ras* mutant mice, we next compared mitochondrial activity of purified cultures of OLs and neurons isolated from *R-Ras* mutant and WT mice. To this

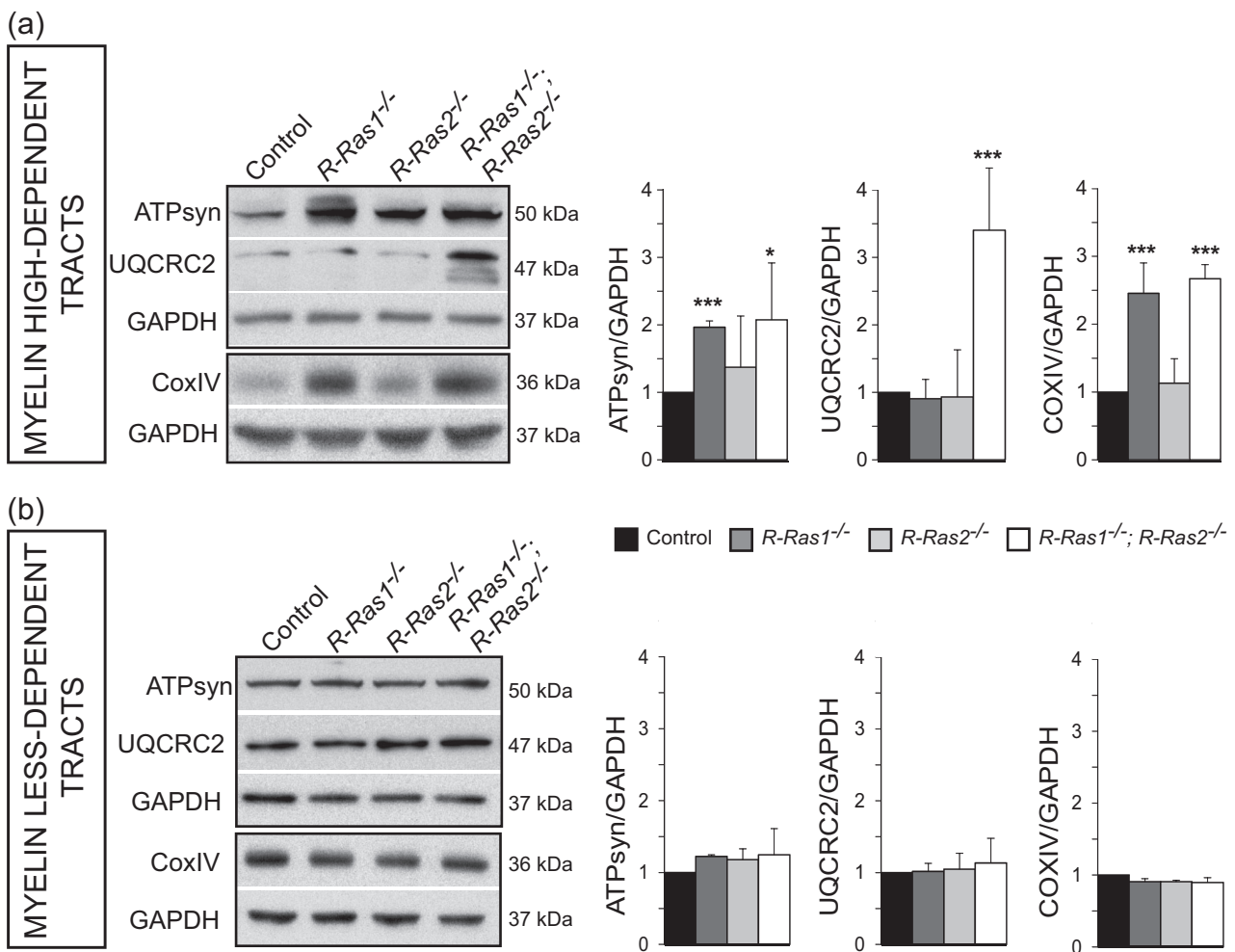


**FIGURE 2** Levels of mitochondrial Complexes III, IV, and V are increased in the absence of *R-Ras1*. (a) Western blot analysis of ATP synthase (Complex V), UQCRC2 (Complex III), and COXIV (Complex IV) in the optic nerve lysates of adult mice (P90) show an increment in the protein levels of these mitochondrial complexes in *R-Ras1*<sup>-/-</sup> single and double-mutants compared to controls, in myelin-dependent tracts. Quantification of western blot evidenced significant increase in mitochondrial Complexes III, IV, and V in *R-Ras1*<sup>-/-</sup> single and double-mutant mice compared to controls. ATP synthase showed significant differences in *R-Ras1*<sup>-/-</sup> (\*\*\* $p < .001$ ) and the double-mutant mice (\* $p < .05$ ). UQCRC2 showed significant differences in the double-mutant mice (\*\*\* $p < .001$ ) compared to the controls. COXIV showed significant differences in *R-Ras1*<sup>-/-</sup> (\*\*\* $p < .001$ ) and the double-mutant mice (\*\*\* $p < .001$ ). (b) Western blot analysis of ATP synthase (Complex V), UQCRC2 (Complex III), and COXIV (Complex IV) in myelin less-dependent tracts lysates of the adult mice (P90) shows no differences in the levels of these mitochondrial complexes in myelin less-dependent tracts. Quantification of western blot did not show any difference in mitochondrial Complexes III (UQCRC2), IV (COXIV), and V (ATP synthase) in single and double-mutant mice compared to controls ( $n = 4$  mice per genotype). Bar graph represents mean  $\pm$  SD of the change, relative to that of controls, in measurements normalized to GAPDH. Two-tailed Student's *t* test was used for the statistical analysis. These experiments were performed three times. GAPDH, glyceraldehyde 3-phosphate dehydrogenase; SD, standard deviation



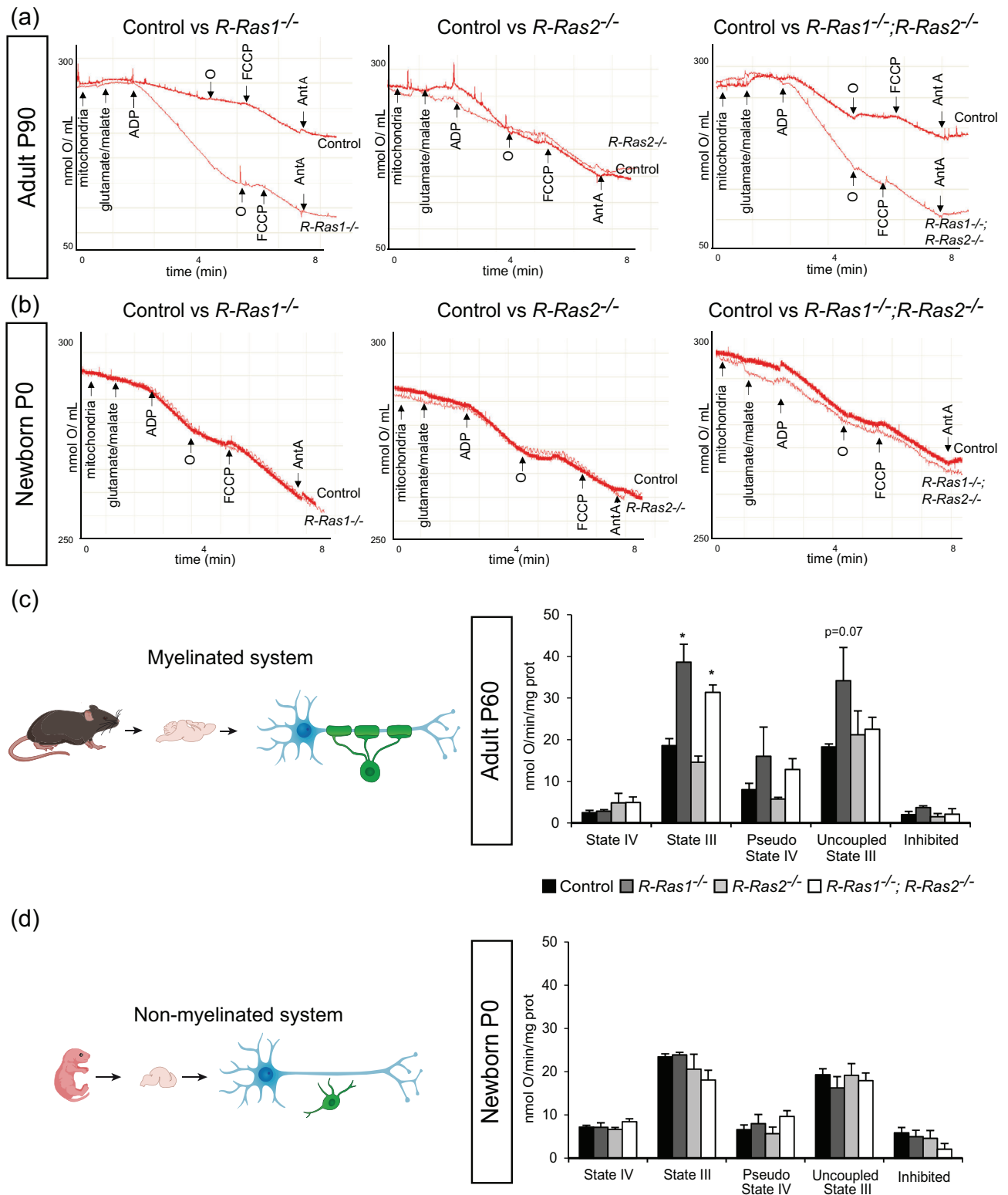


**FIGURE 3** Myelin deficiency in *R-Ras1*<sup>-/-</sup> mice leads to an increase in mitochondrial activity. (a) Polarographic profiles of isolated mitochondria from the brain extracts of controls and mutant adult mice (P90) in the presence of 10 nM glutamate/malate, 0.5 mM ADP, 5  $\mu$ M oligomycin (O), 5  $\mu$ M FCCCP, and 1  $\mu$ M antimycin A (AntA), show evidence of higher mitochondrial activity in *R-Ras1*<sup>-/-</sup> single and double-mutants. (b) Polarographic profiles of isolated mitochondria from the brain extracts of controls and mutant newborn (P0) mice in the presence of 10 nM glutamate/malate, 0.5 mM ADP, 5  $\mu$ M oligomycin (O), 5  $\mu$ M FCCCP, and 1  $\mu$ M AntA, did not show any difference between the mitochondrial activity in single and double-mutants compared to controls. (c) Representative scheme of a myelinated system and graph showing the quantification of Clark-type electrode results in adult (P60) mice mitochondria. State III respiration is expressed in nmol O<sub>2</sub>/min/mg protein. These data show significant differences between *R-Ras1*<sup>-/-</sup> (\**p* < .05) and the double-mutant mice (\**p* < .05). (d) Representative scheme of a nonmyelinated system and graph showing the quantification of Clark-type electrode results in newborn (P0) mice brain mitochondria. State III respiration is expressed in nmol O<sub>2</sub>/min/mg protein. These data did not show any significant differences (*n* = 4 mice per genotype). Two-tailed Student's *t* test was used for the statistical analysis [Color figure can be viewed at [wileyonlinelibrary.com](http://wileyonlinelibrary.com)]

end, we performed Seahorse assays to measure OCR in adherent cultures but did not detect any differences between mutant and control mice in either cell types (Sup. Figure S1a,c,e) and OLs (Sup. Figure S1g,i,k). Results of ATP-coupled respiration in cultured neurons: WT ( $62.4 \pm 9.8$  OCR) versus *R-Ras1KO* ( $66.2 \pm 7.2$  OCR); WT ( $57.6 \pm 23.8$  OCR) versus *R-Ras2KO* ( $69.9 \pm 11.7$  OCR); and WT ( $64.7 \pm 13.1$  OCR) versus DKO ( $71.8 \pm 10.3$  OCR) (Sup. Figure S1b,d,f). Results of maximal respiratory capacity in cultured neurons: WT ( $203.7 \pm 32.1$  OCR) versus *R-Ras1KO* ( $203.4 \pm 19.2$  OCR); WT ( $125.2 \pm 34.8$  OCR) versus *R-Ras2KO* ( $117.9 \pm 25.5$  OCR); and WT ( $96.3 \pm 28.1$  OCR) versus DKO ( $102.1 \pm 17.4$  OCR) (Sup. Figure S1b,d,f). In the case of ATP-coupled

respiration in OLs: WT ( $69.7 \pm 18.4$  OCR) versus *R-Ras1KO* ( $66.0 \pm 19.5$  OCR); WT ( $65.9 \pm 7.1$  OCR) versus *R-Ras2KO* ( $67.2 \pm 13.2$  OCR); and WT ( $66.5 \pm 7.2$  OCR) versus DKO ( $50.9 \pm 12.26$  OCR) (Sup. Figure S1h,j,l). Results of maximal respiratory capacity in OLs: WT ( $105.75 \pm 21.4$  OCR) versus *R-Ras1KO* ( $106.4 \pm 14.2$  OCR); WT ( $91.7 \pm 27.4$  OCR) versus *R-Ras2KO* ( $122.4 \pm 30.6$  OCR); and WT ( $110.0 \pm 31.9$  OCR) versus DKO ( $82.6 \pm 28.5$  OCR) (Sup. Figure S1h,j,l). These results proved the absence of intrinsic mitochondrial alterations within neurons and OLs independently, suggesting that R-Ras1 and R-Ras2 are essential, from a mitochondrial perspective, for correct energetic coupling between the OL and neuron.

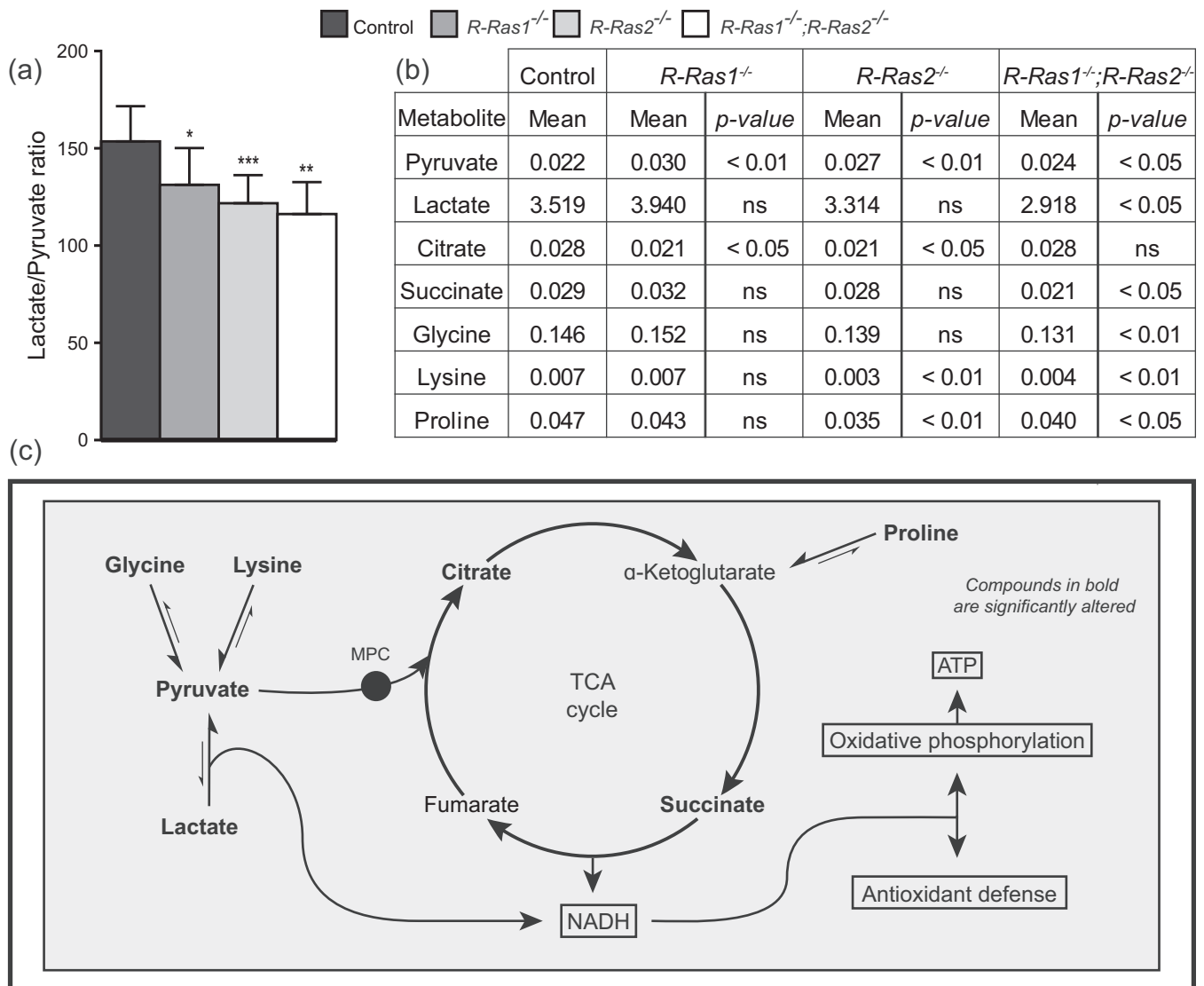


**FIGURE 4** Absence of R-Ras1 and/or R-Ras2 modifies the metabolism in the optic nerve. (a) Lactate/pyruvate ratio is decreased in single and double mutant mice compared to controls. Bar graph represents the mean  $\pm$  SD and shows significant differences in *R-Ras1<sup>-/-</sup>* ( $*p < .05$ ), *R-Ras2<sup>-/-</sup>* ( $***p < .001$ ), and *R-Ras1<sup>-/-</sup>;R-Ras2<sup>-/-</sup>* ( $**p < .01$ ) compared to controls. (b) Table showing the mean area under the curve of metabolites that are significantly altered in *R-Ras* single and double mutants compared to controls. Optic nerve samples were obtained from adult mice (P90) ( $n = 9$  mice per genotype). For the metabolomics statistical analysis, Benjamini and Hochberg and Mann-Whitney *U* tests were used. (c) Schematic representation showing the possible link between the detected altered metabolites and their fate in support of ATP production and antioxidant defense. MPC, mitochondrial pyruvate carrier; SD, standard deviation

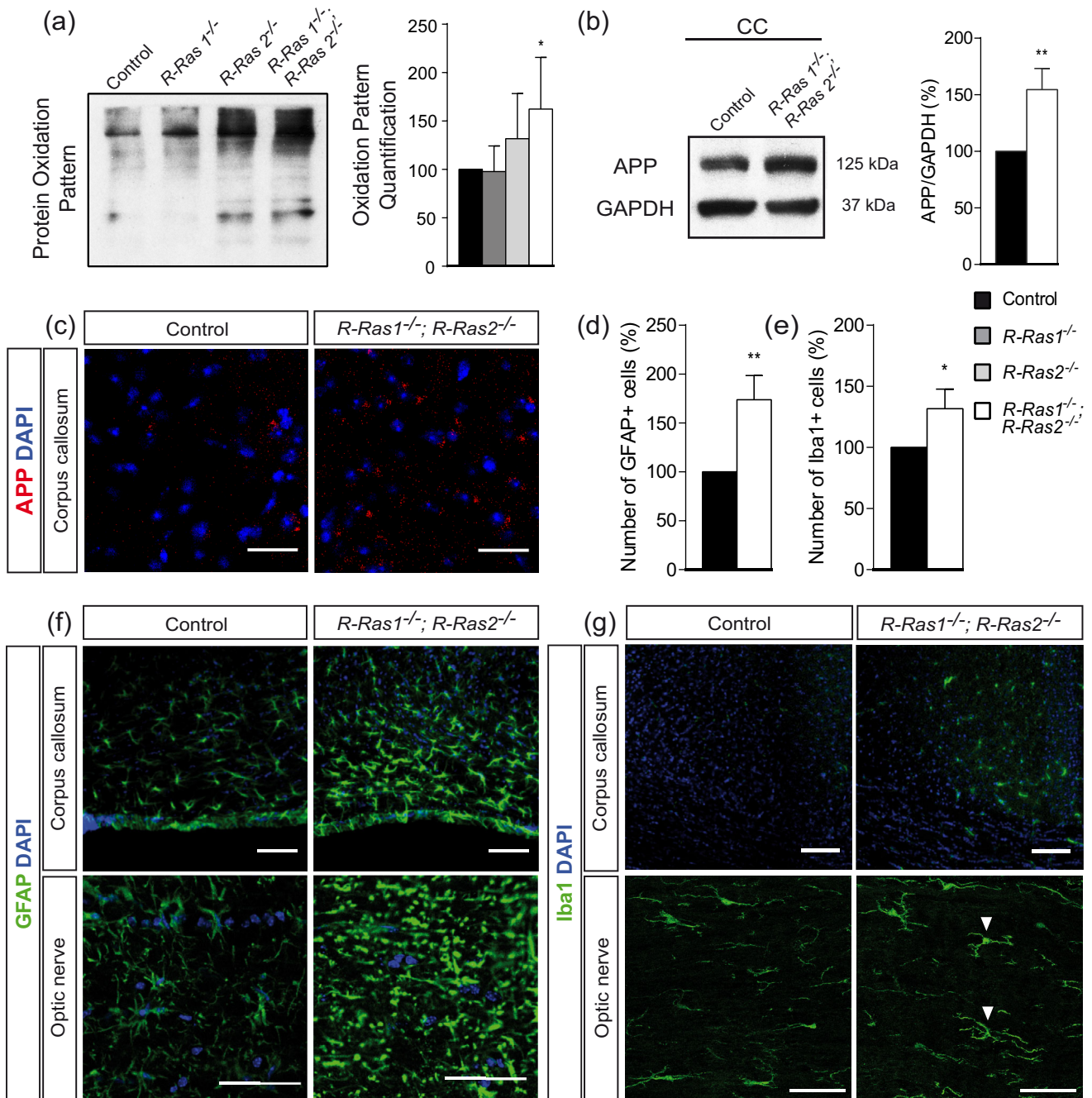


**FIGURE 5** Higher levels of protein oxidation accompanied by APP accumulation, astrogliosis, and microgliosis in *R-Ras1<sup>-/-</sup>;R-Ras2<sup>-/-</sup>* mutant mice. (a) Western blot of the protein oxidation pattern of optic nerve lysates from single and double *R-Ras* mutant adult mice (P90) compared to controls, showing an increase in protein oxidation pattern in the absence of *R-Ras1* and *R-Ras2* (\* $p < .05$ ). (b) Western blot in the cerebral cortex (CC) lysates of adult mice (P90) shows an increase in APP in *R-Ras1<sup>-/-</sup>;R-Ras2<sup>-/-</sup>* relative to controls (\* $p < .05$ ). (c) Confocal microscopy images of the transverse sections of the CC of the adult (P90), immunostained against APP, revealed an increase in APP staining in *R-Ras1<sup>-/-</sup>;R-Ras2<sup>-/-</sup>*. Scale bar, 25  $\mu\text{m}$ . (d) Graph of GFAP positive cells in the corpus callosum shows a significant increase in *R-Ras1<sup>-/-</sup>;R-Ras2<sup>-/-</sup>* mice relative to controls (\*\* $p < .01$ ). (e) Graph of Iba1 positive cells in the corpus callosum shows a significant increase in *R-Ras1<sup>-/-</sup>;R-Ras2<sup>-/-</sup>* mice relative to controls (\* $p < .05$ ). (f) Confocal microscopy images of the transverse sections of the Corpus callosum and the longitudinal sections of the optic nerve of adult mice (P90) immunostained against GFAP, revealed an increase in GFAP staining in *R-Ras1<sup>-/-</sup>;R-Ras2<sup>-/-</sup>* mice relative to controls. Scale bar, 50  $\mu\text{m}$ . (g) Confocal microscopy images of the transverse sections of the corpus callosum and the longitudinal sections of optic nerve of adult mice (P90) immunostained with Iba1, revealed an increase in Iba1 staining in *R-Ras1<sup>-/-</sup>;R-Ras2<sup>-/-</sup>* mice relative to controls. Scale bar, 50  $\mu\text{m}$  ( $n = 3$  mice per genotype). Values in all bar graphs represent the mean  $\pm$  SD of the change, relative to that of controls. Two-tailed Student's *t* test was used for the statistical analysis. APP, amyloid precursor protein; GAPDH, glyceraldehyde 3-phosphate dehydrogenase; GFAP, glial fibrillary acidic protein; Iba1, ionized calcium-binding adapter molecule 1; SD, standard deviation [Color figure can be viewed at [wileyonlinelibrary.com](http://wileyonlinelibrary.com)]



### 3.5 | Absence of R-Ras1 and/or R-Ras2 alters metabolism in myelin-deficient tissues

We next asked in what way the metabolic states of the axons are affected by an increase in number and/or activity of the mitochondria. In answer, we conducted an untargeted metabolomics-based study in the optic nerves of adult mice lacking R-Ras1 and/or R-Ras2, where we identified changes in the concentrations of multiple metabolites with GC-MS.

In R-Ras mutant mice, we found decreased lactate/pyruvate ratios in all R-Ras genotypes, but was most decreased in the DKO mice (WT:  $153.53 \pm 18.11$ ; R-Ras1KO:  $131.21 \pm 18.91$ ,  $p < .05$ ; R-Ras2KO:  $121.75 \pm 14.44$ ,  $p < .001$ ; and DKO:  $116.19 \pm 16.42$ ,  $p < .01$ ) (Figure 4a). Lower lactate/pyruvate ratio confirm increased ATP production in R-Ras mutant mice, which highlight increased mitochondrial function (Arnold & Rustin, 2001; Correia et al., 2006; Robinson, 2006).

We next used the web application MetaboAnalyst, commonly used to integrate metabolomic analysis (Chong et al., 2019), to ask how the changes we had observed in R-Ras1 and/or R-Ras2KO mice affected different steps in the cellular metabolism. We found alterations for pyruvate (control:  $0.022 \pm 0.004$ ; R-Ras1KO:  $0.030 \pm 0.007$ ,  $p < .01$ ; R-Ras2KO:  $0.027 \pm 0.003$ ,  $p < .01$ ; and DKO:  $0.024 \pm 0.003$ ,  $p < .05$ ), lactate (control:  $3.519 \pm 0.640$ ; R-Ras1KO:  $3.940 \pm 0.699$ ; R-Ras2KO:  $3.314 \pm 0.405$ ; and DKO:  $2.918 \pm 0.720$ ,  $p < .05$ ), citrate (control:  $0.028 \pm 0.010$ ; R-Ras1KO:  $0.021 \pm 0.004$ ,  $p < 0.05$ ; R-Ras2KO:  $0.021 \pm 0.004$ ,  $p < 0.05$ ; and DKO:  $0.028 \pm 0.010$ ), succinate (control:  $0.029 \pm 0.007$ ; R-Ras1KO:  $0.032 \pm 0.007$ ; R-Ras2KO:  $0.028 \pm 0.004$ ; and DKO:  $0.021 \pm 0.007$ ,  $p < .05$ ), glycine (control:  $0.146 \pm 0.031$ ; R-Ras1KO:  $0.152 \pm 0.052$ ; R-Ras2KO:  $0.139 \pm 0.057$ ; and DKO:  $0.131 \pm 0.040$ ,  $p < .01$ ), lysine (control:  $0.007 \pm 0.002$ ; R-Ras1KO:  $0.007 \pm 0.002$ ; R-Ras2KO:  $0.003 \pm 0.001$ ,  $p < .01$ ; and DKO:  $0.004 \pm 0.001$ ,  $p < .01$ ), and proline (control:  $0.047 \pm 0.012$ ; R-

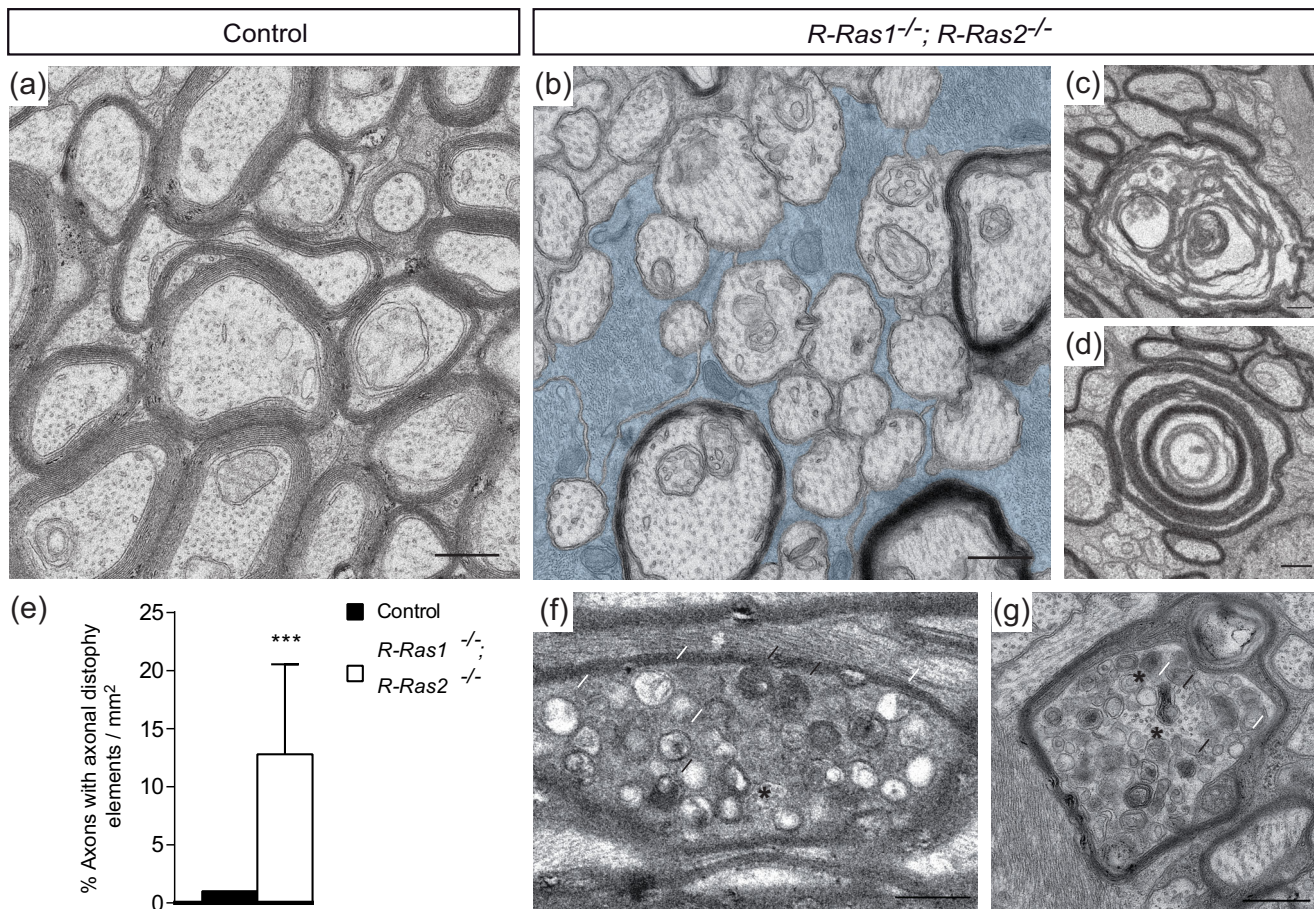


**FIGURE 6** Transmission electron micrographs (TEMs) show astrogliosis and extensive axonal damage in the optic nerves of R-Ras1<sup>-/-</sup>;R-Ras2<sup>-/-</sup> mice. TEM of the optic nerves of controls (a) and R-Ras1<sup>-/-</sup>;R-Ras2<sup>-/-</sup> mice (b), astrogliosis is outlined in blue. R-Ras1<sup>-/-</sup>;R-Ras2<sup>-/-</sup> mice show more degenerating myelin sheaths presumptive of axonal degeneration (c,d). The R-Ras1<sup>-/-</sup>;R-Ras2<sup>-/-</sup> mice present with increased swollen axons (f,g) containing autophagosomes (white arrows), autophagolysosomes (black arrows), and multivesicular bodies (MVBs, black asterisks) relative to control mice. Axons with dystrophy elements were quantified. (e) Bar graph of axons with dystrophy elements/mm<sup>2</sup> showed increased MVBs and autophagy vesicles in the optic nerve of R-Ras1<sup>-/-</sup>;R-Ras2<sup>-/-</sup> mice compared to controls. Bar graph represents the mean  $\pm$  SD (\*\*\*) ( $p < .001$ ). Two-tailed Student's *t* test was used for the statistical analysis. Scale bars: 500 nm. Images were taken at 12,000 $\times$  magnification ( $n = 3$  mice per genotype). SD, standard deviation [Color figure can be viewed at [wileyonlinelibrary.com](http://wileyonlinelibrary.com)]

*Ras1*KO:  $0.043 \pm 0.013$ ; *R-Ras2*KO:  $0.035 \pm 0.011$ ,  $p < .01$ ; and *DKO*:  $0.040 \pm 0.013$ ,  $p < .05$ ) (Figure 4b). Taken together, these data show that several metabolites directly involved in the Krebs cycle metabolism and amino acids are altered in *R-Ras* mutant mice (Figure 4c) in a way that suggest that mitochondria produce more energy relative to controls.

### 3.6 | Absence of R-Ras1 and R-Ras2 leads to the degeneration and loss of axonal function

We next sought to determine whether the increased mitochondrial activity we had observed led to an increase in ROS. To this end, we used a commercially available kit to detect protein oxidation levels in

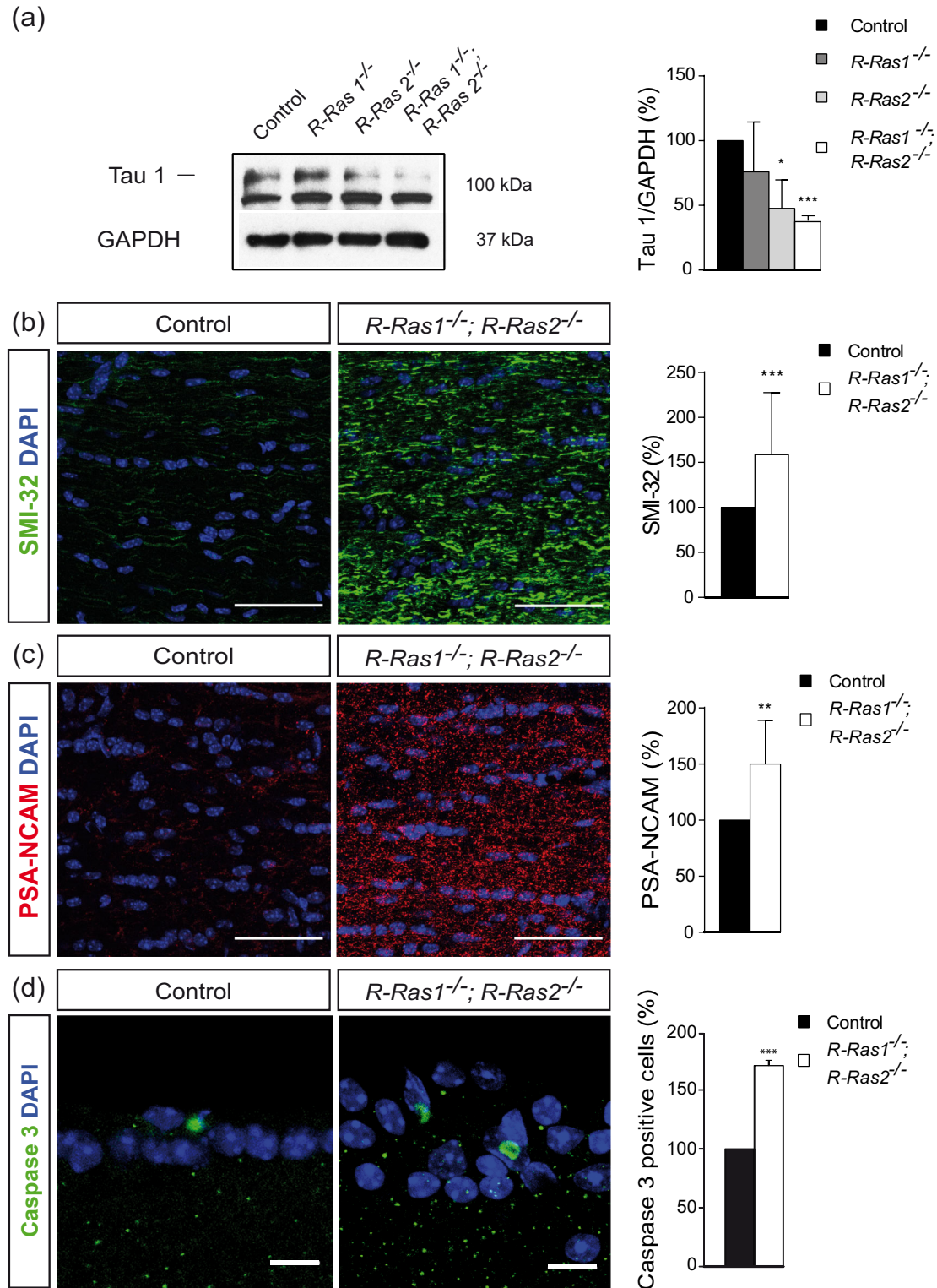


**FIGURE 7** Legend on next page.



optic nerve homogenates from adult mutant mice compared to controls (Figure 5a). Although we did not observe significant differences in the single mutants relative to the WT, we detected the presence of a significantly elevated oxidizing environment in adult *DKO* mice (*R-Ras1KO*:  $97.7 \pm 26.5\%$ ; *R-Ras2KO*:  $131.8 \pm 46.6\%$ ; and *DKO*:  $162.4 \pm 53.4\%$ ,  $p < .05$ ) (Figure 5a).

To know whether the increases in protein oxidation levels generated axonal pathology, we used immunohistochemical staining of the cerebral cortex sections against the APP. The extent of APP protein levels appeared to be correlated with histopathological lesion and thus suggests that APP detection serves as a sensitive marker in myelin diseases (Gehrmann, Banati, Cuzner, Kreutzberg, & Newcombe, 1995). *DKO* mice showed more intense staining compared to controls (Figure 5c). These findings were corroborated by western blot analysis in cerebral cortex homogenates, where we found significantly increased APP in *DKO* mice relative to WT (*DKO*  $154.52 \pm 18.71\%$ ,  $p < .01$ ) (Figure 5b).

To know whether axonal damage was accompanied by astrogliosis or/and microgliosis, we used immunostaining with GFAP and ionized calcium-binding adapter molecule 1 (*Iba1*) in the optic nerve and corpus callosum sections (Figure 5f,g). *DKO* mice showed an increase of  $173.95 \pm 24.71\%$  relative to control ( $p < .01$ ) in GFAP positive cells (Figure 5d). GFAP positive astrocytes from *DKO* mice exhibited morphologic changes characteristic of pathological conditions such as soma and processes hypertrophy (Figure 5f) (Escartin, Guillemaud, & Carrillo-de Sauvage, 2019). In addition, *DKO* mice showed an increase in *Iba1* positive cells of  $131.75 \pm 16.08\%$  relative to control ( $p < .05$ ) (Figure 5e). *DKO* microglia revealed an inflammatory-related morphology (Figure 5g, white arrow heads).

Furthermore, transmission electron micrographs (TEMs) confirmed axonal damage in the optic nerves of *DKO* mice relative to controls (Figure 6a–d,f,g). *DKO* showed increased astrocytic processes compared to WT (Figure 6a,b) (outlined in blue). In addition, *DKO* mice have more degenerating myelin sheaths, presumptive of axonal degeneration and increased swollen axons containing autophagosomes (Figure 6f,g, white arrows), autophagolysosomes (Figure 6f,g, black arrows), and MVBs (Figure 6f,g, black asterisks). Quantification of axonal damage elements showed an increase of

$12.81 \pm 7.74$  per  $\text{mm}^2$  relative to controls ( $p < .001$ ) (Figure 6e). The data above corroborate extensive axonal pathology (Edgar et al., 2009; Ray et al., 2017).

We then asked whether the degree of phosphorylation/dephosphorylation of cytoskeletal elements would allow us to assess how axonal health was affected in *R-Ras* mutant mice. To this end, we performed western blot analysis in single and double mutant adult mice with antibodies for Tau 1, neurofilament heavy chain (NFH) and PSA-NCAM. In optic nerve homogenates, we found that the phosphorylated form of Tau 1 was significantly decreased in *R-Ras2KO* and *DKO* mice relative to WT (*R-Ras1KO*:  $75.9 \pm 38.5\%$ ; *R-Ras2KO*:  $47.7 \pm 22.1\%$ ,  $p < .01$ ; and *DKO*  $37.4 \pm 3.8\%$ ,  $p < .001$ ) (Figure 7a). In the longitudinal optic nerve sections, we identified the non-phosphorylated form of NFH by immunohistochemical staining with the specific SMI-32 antibody (Figure 7b) (Thangavel, Sahu, Van Hoesen, & Zaheer, 2009). Signal quantification revealed a significant increase in axonal dephosphorylation in *DKO* relative to WT mice ( $58.7 \pm 25.5\%$ ,  $p < .001$ ) (Figure 7b). PSA-NCAM is commonly upregulated in myelin diseases (Charles, 2002); we next quantified PSA-NCAM levels by immunohistochemical staining in the longitudinal optic nerve sections. Similar to NFH, PSA-NCAM was significantly increased in *DKO* relative to WT mice ( $50.0 \pm 12.9\%$ ,  $p < .01$ ) (Figure 7c).

To determine whether the axonal damage produced by the increase in protein oxidation compromised the neuronal survivability, we used immunohistochemical staining against active/cleaved caspase-3 in the retinal ganglion cells (RGCs). Histological examination revealed an increase in apoptotic processes in RGCs in *DKO* ( $169.02 \pm 4.47\%$ ,  $p < .001$ ) relative to controls (Figure 7d).

Cumulatively, the increase in APP, GFAP, *Iba1*, and PSA-NCAM protein levels, and changes in the phosphorylation levels of the axonal cytoskeleton, together with the apoptotic processes, suggests the presence of axonal degeneration and neuronal loss in the double mutants.

To evaluate whether these alterations had functional consequences, we performed optokinetic reflex measurements, a test commonly used to evaluate retinal function in retinal degeneration mouse models, in controls and *R-Ras* mutant mice. In this assay, experimental animals were placed in an environment with a screen simulating

**FIGURE 7** Absence of *R-Ras1* and *R-Ras2* causes the loss of integrity in the axonal cytoskeleton components associated with neuronal death. (a) Western blot of Tau 1 in the optic nerve lysates of adult mice (P90), showing a significant reduction in the Tau 1 phosphorylated isoform in *R-Ras2<sup>-/-</sup>* and *R-Ras1<sup>-/-</sup>;R-Ras2<sup>-/-</sup>* mice compared with controls. These experiments were performed three times and results were normalized to GAPDH. Results show significant decrease in *R-Ras2<sup>-/-</sup>* ( $*p < .05$ ) and *R-Ras1<sup>-/-</sup>;R-Ras2<sup>-/-</sup>* ( $***p < .001$ ). (b) Confocal microscopy images of the longitudinal sections of the optic nerves of adult mice (P90) immunostained with SMI-32 revealed an increase in staining in *R-Ras1<sup>-/-</sup>;R-Ras2<sup>-/-</sup>* mice relative to controls. Graph of SMI-32 mean fluorescence quantification showing a significant increase in double mutant mice compared to controls ( $***p < .001$ ). Scale bar, 50  $\mu\text{m}$ . (c) Confocal microscopy images of the longitudinal sections of the optic nerves of adult mice (P90) immunostained with PSA-NCAM, revealed an increase in PSA-NCAM staining in *R-Ras1<sup>-/-</sup>;R-Ras2<sup>-/-</sup>* mice relative to controls. Graph of PSA-NCAM mean fluorescence quantification showing a significant increase in double mutant mice compared to controls ( $**p < .01$ ). Scale bar, 50  $\mu\text{m}$ . (d) Confocal microscopy images of the transverse sections of the retina of adult mice (P90) immunostained with cleaved caspase 3, revealed an increase in caspase 3 positive cells in *R-Ras1<sup>-/-</sup>;R-Ras2<sup>-/-</sup>* mice relative to controls. Scale bar, 10  $\mu\text{m}$ . Histological examination revealed an increase in apoptotic processes in the retinal ganglion cells (RGCs) in *R-Ras1<sup>-/-</sup>;R-Ras2<sup>-/-</sup>* ( $***p < .001$ ). ( $n = 3$  mice per genotype). Bar graph represents the mean  $\pm$  SD of the change as percentage, relative to the controls measurements. Two-tailed Student t test was used for the statistical analysis. GAPDH, glyceraldehyde 3-phosphate dehydrogenase; PSA-NCAM, polysialylated-neural cell adhesion molecule; SD, standard deviation [Color figure can be viewed at [wileyonlinelibrary.com](http://wileyonlinelibrary.com)]

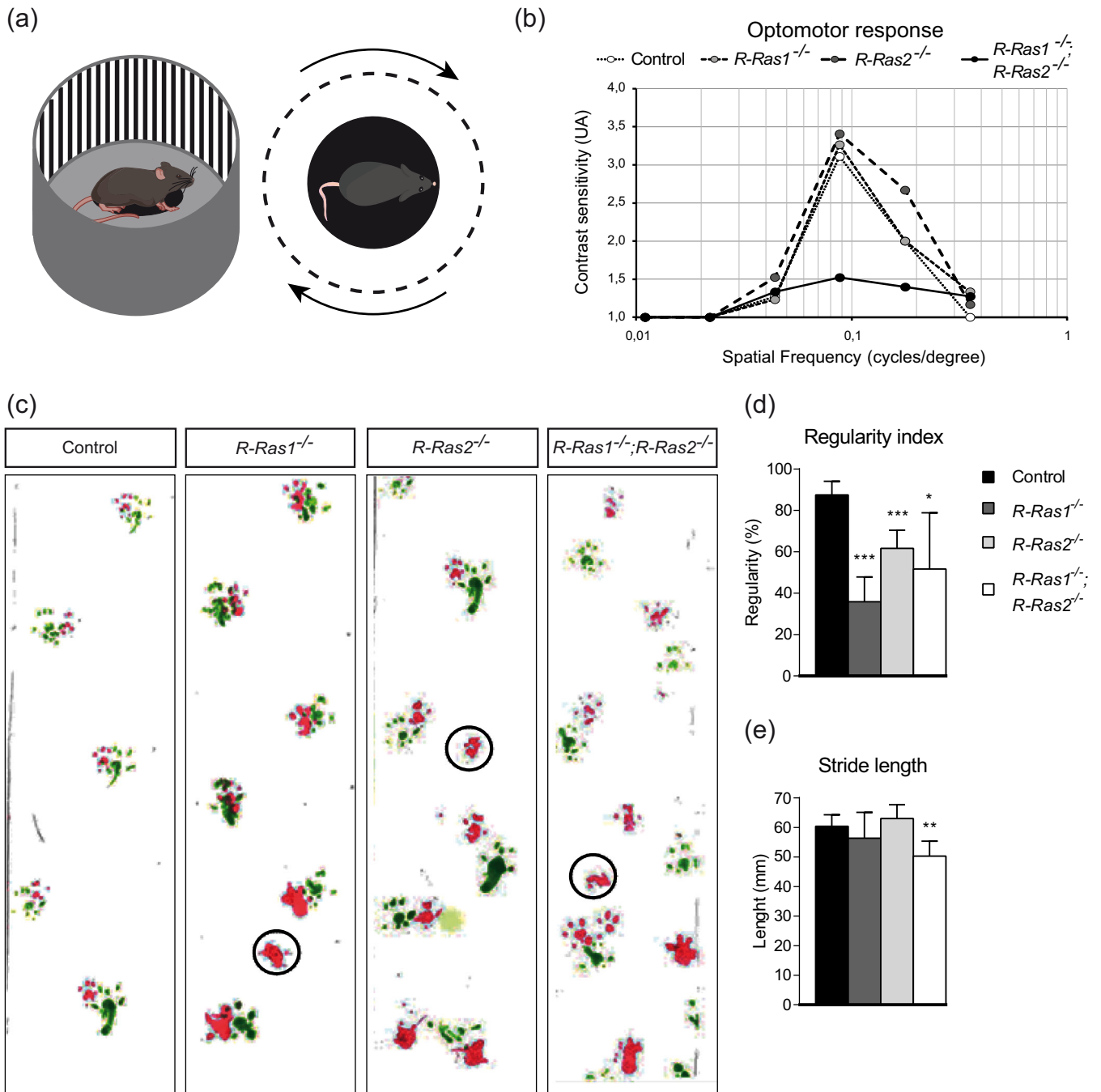


**FIGURE 8** Absence of R-Ras1 and R-Ras2 leads to loss of function. (a) Schematic representation of optomotor response test. (b) Graph of optokinetic responses of controls, *R-Ras1*<sup>-/-</sup>, *R-Ras2*<sup>-/-</sup> and *R-Ras1*<sup>-/-</sup>; *R-Ras2*<sup>-/-</sup> mice. Statistical differences between the double mutant and control mice (\*\*p < .001) were found for intermediate spatial frequencies: 0.088, and 0.177 cycles/°. No significant statistical differences were found between single mutant and control animals. Contrast sensitivity is represented as a function of spatial frequency as the mean ± SD. All experiments were performed in adult mice (P90) (n = 8 mice per genotype). Analysis of variance (ANOVA) and Bonferroni post test were used for statistical analysis. (c) Gait study reveals moderate motor impairment in *R-Ras1*<sup>-/-</sup>, *R-Ras2*, and *R-Ras1*<sup>-/-</sup>; *R-Ras2*<sup>-/-</sup> mice. Images show forepaw prints in pink and hindpaw prints in green. Circles indicate missteps affecting mostly the forelimbs. (d) Gait analysis indicates low regularity index due to missteps in *R-Ras1*<sup>-/-</sup> (\*\*p < .001), *R-Ras2*<sup>-/-</sup> (\*\*p < .001), and *R-Ras1*<sup>-/-</sup>; *R-Ras2*<sup>-/-</sup> (\*p < .05) compared to controls. (e) Stride length analysis reveals a decrease in stride length in *R-Ras1*<sup>-/-</sup>; *R-Ras2*<sup>-/-</sup> (\*\*p < .01) mice compared to controls (n = 5 mice per genotype). Two-tailed Student's t test was used for the statistical analysis. SD, standard deviation [Color figure can be viewed at [wileyonlinelibrary.com](http://wileyonlinelibrary.com)]

rotating black and white vertical bars, and in which their characteristic head reflex movements in the same direction as the rotating bars were measured (Figure 8a). Contrast sensitivity was used to assess

the degree of capacity for visual discrimination. We found that reflex responses induced by the bar rotation at different spatial frequencies were significantly lower in DKO mice relative to both single mutants



and control animals (Figure 8b). Specifically, contrast sensitivity in the range of 0.011–0.355 cycles/° was significantly weaker in *DKO* mice ( $p < .001$ ), indicating a strong visual impairment (Figure 8b).

To confirm how axonal degeneration affected other strongly myelin-dependent regions such as the spinal cord, we evaluated single and double mutant mice motor function by paw-print tests (Maggipinto et al., 2017). Single and double mutant mice showed modifications in the gait regularity, including new erratic footsteps (Figure 8c, circle paws). Percentage of correct step sequences over the total number of step cycles were: for control:  $87.50 \pm 6.66$ ; *R-Ras1KO*:  $35.87 \pm 11.98$  ( $p < .001$ ); *R-Ras2KO*:  $61.67 \pm 8.81$  ( $p < .001$ ); and *DKO*:  $51.66 \pm 27.23$  ( $p < .05$ ) (Figure 8d). In addition, *DKO* showed a decrease in stride length (control:  $60.37 \pm 3.93$  mm and *DKO*:  $50.30 \pm 5.08$  mm ( $p < .05$ ) (Figure 8e).

Taken together, these findings suggest that myelin deficiency caused by the loss of R-Ras1 and R-Ras2 leads to increased ROS levels, which in turn causes severe axonal degeneration and loss of function.

## 4 | DISCUSSION

Our previous work demonstrated that R-Ras1 and R-Ras2 are essential for the correct myelination of the CNS by safeguarding survival and differentiation of OLs. Although single mutant adult mice had moderate degrees of hypomyelination, *DKO* mice had a dramatic lack of myelin. Stalled OL maturation lead to hypomyelination, with shorter sheaths and increased Nodes of Ranvier numbers, causing a slowdown in nerve impulse transmission (Sanz-Rodríguez et al., 2018). It is known that myelin deficits increases the number of Nodes of Ranvier and alters the distribution of  $\text{Na}^+$  channels along the hypomyelinated axonal surface (Craner, Newcombe, et al., 2004; Hunanyan et al., 2011; Savvaki et al., 2008). To compensate for this anomaly, energy demands within the axon increases (Campbell & Mahad, 2012; Stys, 2005). Since mitochondria are responsible for cellular energy metabolism through the Krebs cycle and OXPHOS, it falls to these organelles to meet the increased need in cellular energy demand. Increase in mitochondrial number and activity are both strategies by which hypomyelinated systems can offset increased energy demands (de Barcelos, Troxell, & Graves, 2019). Autopsy studies on patients with MS show evidence of mitochondrial adaptations (Mahad et al., 2009; Witte et al., 2009; Zamboni et al., 2011). These increases in energy demands affect the cellular metabolism. High levels of pyruvate reflect an increase in NADH routed to enhance ATP production. In single and double mutants, the Krebs cycle metabolites are reduced, suggesting a chemical equilibrium shift towards increasing NADH production to obtain energy. Given the lack of myelin in R-Ras mutant mice, high energy demand situations could require amino acid degradation to fuel the Krebs cycle. All these data are supported by the lower lactate/pyruvate ratio present in single and double mutant mice, a biomarker of mitochondrial function, used in the diagnosis of mitochondrial disorders (Arnold & Rustin, 2001; Chinnery, 2014; Correia et al., 2006; Robinson, 2006).

Cumulatively, our data show that the absence of R-Ras1 and/or R-Ras2 increases energy demands in hypomyelinated tracts, resulting in metabolic adaptations to increase ATP production. Despite the fact that R-Ras1 and R-Ras2 are essential in myelination processes (Sanz-Rodríguez et al., 2018), here we also found differences in how single R-Ras mutants compensated to mitigate effects of myelin deficiency. One possible explanation may be that hypomyelination is compensated in a different manner depending on its degree. Other possible explanation is that R-Ras1 and R-Ras2 do not perform redundant functions, suggesting functional specialization for each. Despite their high homology, several literatures exist to support that R-Ras1 loss cannot be compensated by R-Ras2 and vice-versa (Iwasawa, Negishi, & Oinuma, 2012; Singh et al., 2012; Yan et al., 2015). Based on the current knowledge and our own results, we consider that R-Ras1 and R-Ras2 have specific, cooperative, and nonredundant functions.

Mice lacking R-Ras1 showed an increase in the levels of mitochondrial complexes and mitochondrial activity in strongly myelin-dependent tissues. In contrast, the absence of R-Ras2 increased the number of mitochondria specifically in those axons that had lost their myelin sheath. Surprisingly, R-Ras2 deficient mice did not show an increase in levels of OXPHOS complexes.

The *DKO* mice presented the most dramatic phenotype with the combination of single mutant specific alterations, sometimes exacerbated, and clear evidence of neuronal degeneration. In *DKO* mice, with a total lack of myelin on most of its axons, mitochondrial numbers and activity were both increased. Since these anomalies were only detected in axons destined to be myelinated, with no effects observed in myelin-independent axons, our results suggest that myelin deficiency and increases in energy demands causes the mitochondrial abnormalities observed in mice lacking R-Ras1 and/or R-Ras2. In agreement with our results, in a model of Pelizaeus–Merzbacher disease, redox imbalance and oxidative damage were found to be due to enhanced ATP production. In this hypomyelinating leukodystrophy model, increased mitochondrial numbers, OXPHOS and Krebs cycle protein levels were also described (Ruiz et al., 2018). In addition, several studies in humans have demonstrated increased content of mitochondrial proteins in unmyelinated axons (Balaratnasingam, Morgan, Johnstone, Cringle, & Yu, 2009). The increment on mitochondrial density would supply the high energy requirements for electrical conduction (Barron, Griffiths, Turnbull, Bates, & Nichols, 2004; Campbell & Mahad, 2012).

The Seahorse experiments performed on purified cultures of mutant OLs or neurons exhibited no mitochondrial defect in these cell types separately, suggesting the mitochondrial effects are caused directly by defects in the myelination processes. However, we cannot rule out that R-Ras1 and/or R-Ras2 have an autonomous cellular mitochondrial effect in OLs or in mature neurons. Unfortunately, the Seahorse experiments do not allow cultures of OLs or neurons for longer times. We are aware that it is necessary to understand the functional role of R-Ras1 and R-Ras2 in neurons, and we intend to clarify the contribution of each cell type to the myelination processes in future works.

Our findings show that R-Ras loss results in increased mitochondrial numbers and activity that create a pro-oxidative environment

with increased ROS levels. Alterations in the mitochondrial size can be explained by the alterations in mitochondrial fission processes, which are common under stress conditions (Youle & van der Bliek, 2012). In this sense, elevated ROS levels can explain the smaller mitochondrial size in *R-Ras2KO* and *DKO* (Cid-Castro, Hernández-Espinosa, & Morán, 2018). These changes, in turn, lead to protein carboxylation contributing to degeneration and axonal dysfunction, which is more pronounced in *R-Ras2KO* and *DKO* mice. Earlier studies have described increased ROS production in the nonmyelinated CNS of patients with MS (Choi et al., 2018; Pandit, Vadnal, Houston, Freeman, & McDonough, 2009; Witte et al., 2013). Furthermore, in vivo experiments demonstrate that attenuation of ROS levels can improve axonal function in mice (Caldeira Da Silva, Cerqueira, Barbosa, Medeiros, & Kowaltowski, 2008; Kapoor, Davies, Blaker, Hall, & Smith, 2003).

Astro- and microgliosis, GFAP, Iba1, and APP immunostainings confirmed the axonal pathology. These data were additionally supported by the TEM studies showing axonal swellings with autophagosomes, autophagolysosomes, and MVBs (Edgar et al., 2009; Escartin et al., 2019; Ray et al., 2017; Yan et al., 2014). All these results strongly suggest a response to pathological stimuli in the presence of ROS. Also, we found that high levels of ROS correlate with abnormalities in the neuronal cytoskeleton as evidenced by alterations in Tau phosphorylation or neurofilaments, well-known essential components in axonal physiology (Thangavel et al., 2009). Increases in SMI-32 protein levels and alterations in Tau phosphorylation also indicated axonal degeneration. This axonal pathology was even revealed in *DKO* mice by PSA-NCAM, an adhesion molecule that is expressed on the axonal surface in nonmyelinating lesions typical in patients with MS (Charles, 2002). Taken together, these data clearly show severe axonal damage in mice lacking *R-Ras1* and *R-Ras2* and explain the degeneration of the axons and neuronal loss in these mice.

Since optic nerve involvement commonly occurs in myelin diseases, evaluation of vision loss is used to estimate axonal function. Optokinetic studies in single and *DKO* mice confirmed alterations of visual function associated with the loss of RGC in the absence of *R-Ras1* and *R-Ras2*. Motor studies of the spinal cord showed functional defects in single and mutant mice in this strongly myelin-dependent region (Benedict et al., 2011; Mandolesi et al., 2019). These results indicate that the alterations in single mutant mice entailed the loss of function.

In summary, this study confirms the hypothesis that the lack of myelin in *R-Ras1KO* and/or *R-Ras2KO* mice causes a chronic increase in energy demand and mitochondrial ATP production. After reaching a critical point, the mitochondria are unable to provide the energy needed for the maintenance of the nerve impulse transmission along hypomyelinated axons. Given this mitochondrial imbalance, ROS levels increase, causing the degeneration of the hypomyelinated axons and a loss of their function. An absence of *R-Ras1* and/or *R-Ras2* reproduces very important aspects of dysmyelinating diseases, such as a decrease in the OL population, a drastic lack of myelin, mitochondrial and metabolic alterations, and axonal degeneration and neuronal loss. For this reason, we propose our *R-Ras* knockout model as a new tool for the study of these diseases.

## ACKNOWLEDGMENTS

This work was supported by the Spanish Ministry of Economy and Competitiveness (RTI2018-096303B-C33) to B. C., (RTI2018-

096303B-C31) to F. W., and RTI2018-095166B-I00 to C. G. R. and P. L. and Instituto de Salud Carlos III and co-funded by the European Regional Development Fund (ERDF) within the "Plan Estatal de Investigación Científica y Técnica y de Innovación 2017–2020" (RD16/0008/0020; FIS/PI 18-00754) to P. div.-P. The authors wish to thank Dr J. De Felipe for his scientific advice. The authors also wish to thank Dr J. M. Cardenas for the statistical support. The authors also want to thank Dr J. Ávila for providing us with the Tau 1 antibody; S. Gutierrez-Erlandsson, M. Guerra, and MT. Rejas for their technical assistance; and NGS Core Facility at the Centro de Biología Molecular Severo Ochoa, Madrid, Spain.

## CONFLICT OF INTEREST

The authors declare no conflict of interest.

## DATA AVAILABILITY STATEMENT

The data that support the findings of this study are available upon reasonable request.

## ORCID

Beatriz Cubelos  <https://orcid.org/0000-0002-2280-8233>

## REFERENCES

- Andrews, H., White, K., Thomson, C., Edgar, J., Bates, D., Griffiths, I., ... Nichols, P. (2006). Increased axonal mitochondrial activity as an adaptation to myelin deficiency in the shiverer mouse. *Journal of Neuroscience Research*, 83(8), 1533–1539. <https://doi.org/10.1002/jnr.20842>
- Arnold, M., & Rustin, P. (2001). Clinical spectrum and diagnosis of mitochondrial disorders. *American Journal of Medical Genetics - Seminars in Medical Genetics*, 106(1), 4–17. <https://doi.org/10.1002/ajmg.1391>
- Balaratnasingam, C., Morgan, W. H., Johnstone, V., Cringle, S. J., & Yu, D. Y. (2009). Heterogeneous distribution of axonal cytoskeleton proteins in the human optic nerve. *Investigative Ophthalmology and Visual Science*, 50(6), 2824–2838. <https://doi.org/10.1167/iov.08-3206>
- Barron, M. J., Griffiths, P., Turnbull, D. M., Bates, D., & Nichols, P. (2004). The distributions of mitochondria and sodium channels reflect the specific energy requirements and conduction properties of the human optic nerve head. *British Journal of Ophthalmology*, 88(2), 286–290. <https://doi.org/10.1136/bjo.2003.027664>
- Benedict, R. H. B., Holtzer, R., Motl, R. W., Foley, F. W., Kaur, S., Hojnacki, D., & Weinstock-Guttman, B. (2011). Upper and lower extremity motor function and cognitive impairment in multiple sclerosis. *Journal of the International Neuropsychological Society*, 17(4), 643–653. <https://doi.org/10.1017/S1355617711000403>
- Boespflug-Tanguy, O., Labauge, P., Fogli, A., & Vaurs-Barriere, C. (2008). Genes involved in leukodystrophies: A glance at glial functions. *Current Neurology and Neuroscience Reports*, 8(3), 217–229. <https://doi.org/10.1007/s11910-008-0034-x>
- Caldeira Da Silva, C. C., Cerqueira, F. M., Barbosa, L. F., Medeiros, M. H. G., & Kowaltowski, A. J. (2008). Mild mitochondrial uncoupling in mice affects energy metabolism, redox balance and longevity. *Aging Cell*, 7(4), 552–560. <https://doi.org/10.1111/j.1474-9726.2008.00407.x>
- Campbell, G. R., & Mahad, D. J. (2012). Mitochondrial changes associated with demyelination: Consequences for axonal integrity. *Mitochondrion*, 12(2), 173–179. <https://doi.org/10.1016/j.mito.2011.03.007>
- Charles, P. (2002). Re-expression of PSA-NCAM by demyelinated axons: An inhibitor of remyelination in multiple sclerosis? *Brain*, 125(9), 1972–1979. <https://doi.org/10.1093/brain/awf216>
- Chinnery, P. F. (2014). Mitochondrial disorders overview summary genetic counseling. *Gene Reviews*, 1–21 Retrieved from [https://www.dropbox.com/s/92278owgu4ewxeu/Bookshelf\\_NBK1224.pdf?dl=0](https://www.dropbox.com/s/92278owgu4ewxeu/Bookshelf_NBK1224.pdf?dl=0)





- Choi, I. Y., Lee, P., Adany, P., Hughes, A. J., Belliston, S., Denney, D. R., & Lynch, S. G. (2018). In vivo evidence of oxidative stress in brains of patients with progressive multiple sclerosis. *Multiple Sclerosis Journal*, 24(8), 1029–1038. <https://doi.org/10.1177/1352458517711568>
- Chong, J., Wishart, D. S., & Xia, J. (2019). Using MetaboAnalyst 4.0 for comprehensive and integrative metabolomics data analysis. *Current Protocols in Bioinformatics*, 68(1), 1–128. <https://doi.org/10.1002/cpbi.86>
- Cid-Castro, C., Hernández-Espinoso, D. R., & Morán, J. (2018). ROS as regulators of mitochondrial dynamics in neurons. *Cellular and Molecular Neurobiology*, 38(5), 995–1007. <https://doi.org/10.1007/s10571-018-0584-7>
- Colicelli, J. (2004). Human RAS superfamily proteins and related GTPases. *Science's STKE*, 2004(250), 1–32. <https://doi.org/10.1126/stke.2502004re13>
- Correia, C., Coutinho, A. M., Diogo, L., Grazina, M., Marques, C., Miguel, T., ... Vicente, A. M. (2006). Brief report: High frequency of biochemical markers for mitochondrial dysfunction in autism: No association with the mitochondrial aspartate/glutamate carrier SLC25A12 gene. *Journal of Autism and Developmental Disorders*, 36(8), 1137–1140. <https://doi.org/10.1007/s10803-006-0138-6>
- Craner, M. J., Hains, B. C., Lo, A. C., Black, J. A., & Waxman, S. G. (2004). Co-localization of sodium channel Nav1.6 and the sodium-calcium exchanger at sites of axonal injury in the spinal cord in EAE. *Brain*, 127(2), 294–303. <https://doi.org/10.1093/brain/awh032>
- Craner, M. J., Newcombe, J., Black, J. A., Hartle, C., Cuzner, M. L., & Waxman, S. G. (2004). Molecular changes in neurons in multiple sclerosis: Altered axonal expression of Nav1.2 and Nav1.6 sodium channels and Na<sup>+</sup>/Ca<sup>2+</sup> exchanger. *Proceedings of the National Academy of Sciences of the United States of America*, 101(21), 8168–8173. <https://doi.org/10.1073/pnas.0402765101>
- de Barcelos, I. P., Troxell, R. M., & Graves, J. S. (2019). Mitochondrial dysfunction and multiple sclerosis. *Biology*, 8(2) 254–271. <https://doi.org/10.3390/biology8020037>
- Delgado, P., Cubelos, B., Calleja, E., Martínez-Martín, N., Ciprés, A., Mérida, I., ... Alarcón, B. (2009). Essential function for the GTPase TC21 in homeostatic antigen receptor signaling. *Nature Immunology*, 10(8), 880–888. <https://doi.org/10.1038/ni.1749>
- Edgar, J. M., McLaughlin, M., Werner, H. B., McCulloch, M. C., Barrie, J. A., Brown, A., ... Griffiths, I. R. (2009). Early ultrastructural defects of axons and axon-glia junctions in mice lacking expression of Cnp1. *Glia*, 57(16), 1815–1824. <https://doi.org/10.1002/glia.20893>
- Escartin, C., Guillemaud, O., & Carrillo-de Sauvage, M. A. (2019). Questions and (some) answers on reactive astrocytes. *Glia*, 67(12), 2221–2247. <https://doi.org/10.1002/glia.23687>
- Figlia, G., Gerber, D., & Suter, U. (2018). Myelination and mTOR. *Glia*, 66(4), 693–707. <https://doi.org/10.1002/glia.23273>
- Foerster, S., Hill, M. F. E., & Franklin, R. J. M. (2019). Diversity in the oligodendrocyte lineage: Plasticity or heterogeneity? *Glia*, 67(10), 1797–1805. <https://doi.org/10.1002/glia.23607>
- Foster, A. Y., Bujalka, H., & Emery, B. (2019). Axoglial interactions in myelin plasticity: Evaluating the relationship between neuronal activity and oligodendrocyte dynamics. *Glia*, 67(11), 2038–2049. <https://doi.org/10.1002/glia.23629>
- Gaesser, J. M., & Fyffe-Maricich, S. L. (2016). Intracellular signaling pathway regulation of myelination and remyelination in the CNS. *Experimental Neurology*, 283, 501–511. <https://doi.org/10.1016/j.expneurol.2016.03.008>
- Gehrmann, J., Banati, R. B., Cuzner, M. L., Kreutzberg, G. W., & Newcombe, J. (1995). Amyloid precursor protein (APP) expression in multiple sclerosis lesions. *Glia*, 15(2), 141–151. <https://doi.org/10.1002/glia.440150206>
- Gonzalez-Riano, C., Sanz-Rodríguez, M., Escudero-Ramirez, J., Lorenzo, M. P., Barbas, C., Cubelos, B., & Garcia, A. (2018). Target and untargeted GC-MS based metabolomic study of mouse optic nerve and its potential in the study of neurological visual diseases. *Journal of Pharmaceutical and Biomedical Analysis*, 153, 44–56. <https://doi.org/10.1016/j.jpba.2018.02.015>
- Guardiola-Diaz, H. M., Ishii, A., & Bansal, R. (2012). Erk1/2 MAPK and mTOR signaling sequentially regulates progression through distinct stages of oligodendrocyte differentiation. *Glia*, 60(3), 476–486. <https://doi.org/10.1002/glia.22281>
- Hill, R. A., & Grutzendler, J. (2019). Uncovering the biology of myelin with optical imaging of the live brain. *Glia*, 67(11), 2008–2019. <https://doi.org/10.1002/glia.23635>
- Hunanyan, A. S., Alessi, V., Pate, S., Pearse, D. D., Matthews, G., & Arvanian, V. L. (2011). Alterations of action potentials and the localization of nav1.6 sodium channels in spared axons after hemisection injury of the spinal cord in adult rats. *Journal of Neurophysiology*, 105(3), 1033–1044. <https://doi.org/10.1152/jn.00810.2010>
- Ishii, A., Furusho, M., Dupree, J. L., & Bansal, R. (2014). Role of ERK1/2 MAPK signaling in the maintenance of myelin and axonal integrity in the adult CNS. *Journal of Neuroscience*, 34(48), 16031–16045. <https://doi.org/10.1523/JNEUROSCI.3360-14.2014>
- Ishii, A., Furusho, M., Macklin, W., & Bansal, R. (2019). Independent and cooperative roles of the Mek/ERK1/2-MAPK and PI3K/Akt/mTOR pathways during developmental myelination and in adulthood. *Glia*, 67(7), 1277–1295. <https://doi.org/10.1002/glia.23602>
- Iwasawa, N., Negishi, M., & Oinuma, I. (2012). R-Ras controls axon branching through afadin in cortical neurons. *Molecular Biology of the Cell*, 23(14), 2793–2804. <https://doi.org/10.1091/mbc.E12-02-0103>
- Kapoor, R., Davies, M., Blaker, P. A., Hall, S. M., & Smith, K. J. (2003). Blockers of sodium and calcium entry protect axons from nitric oxide-mediated degeneration. *Annals of Neurology*, 53(2), 174–180. <https://doi.org/10.1002/ana.10443>
- Katsu-Jiménez, Y., & Giménez-Cassina, A. (2019). Fibroblast growth factor-21 promotes ketone body utilization in neurons through activation of AMP-dependent kinase. *Molecular and Cellular Neuroscience*, 101(October), 103415. <https://doi.org/10.1016/j.mcn.2019.103415>
- Lee, Y., Morrison, B. M., Li, Y., Lengacher, S., Farah, M. H., Hoffman, P. N., ... Rothstein, J. D. (2012). Oligodendroglia metabolically support axons and contribute to neurodegeneration. *Nature*, 487(7408), 443–448. <https://doi.org/10.1038/nature11314>
- Lüders, K. A., Nessler, S., Kusch, K., Patzig, J., Jung, R. B., Möbius, W., ... Werner, H. B. (2019). Maintenance of high proteolipid protein level in adult central nervous system myelin is required to preserve the integrity of myelin and axons. *Glia*, 67(4), 634–649. <https://doi.org/10.1002/glia.23549>
- Maggipinto, M. J., Ford, J., Le, K. H., Tutolo, J. W., Furusho, M., Wizeman, J. W., ... Barbarese, E. (2017). Conditional knockout of TOG results in CNS hypomyelination. *Glia*, 65(3), 489–501. <https://doi.org/10.1002/glia.23106>
- Mahad, D. J., Ziabreva, I., Campbell, G., Lax, N., White, K., Hanson, P. S., ... Turnbull, D. M. (2009). Mitochondrial changes within axons in multiple sclerosis. *Brain*, 132(5), 1161–1174. <https://doi.org/10.1093/brain/awp046>
- Mandolesi, G., Bullitta, S., Fresegna, D., de Vito, F., Rizzo, F. R., Musella, A., ... Gentile, A. (2019). Voluntary running wheel attenuates motor deterioration and brain damage in cuprizone-induced demyelination. *Neurobiology of Disease*, 129(July 2018), 102–117. <https://doi.org/10.1016/j.nbd.2019.05.010>
- Murcia-Belmonte, V., Esteban, P. F., Martínez-Hernández, J., Gruart, A., Luján, R., Delgado-García, J. M., & de Castro, F. (2016). Anosmin-1 over-expression regulates oligodendrocyte precursor cell proliferation, migration and myelin sheath thickness. *Brain Structure and Function*, 221(3), 1365–1385. <https://doi.org/10.1007/s00429-014-0977-4>
- Murcia-Belmonte, V., Medina-Rodríguez, E. M., Bribián, A., de Castro, F., & Esteban, P. F. (2014). ERK1/2 signaling is essential for the chemotaxis exerted by human FGF2 and human anosmin-1 on newborn rat and mouse OPCs via FGFR1. *Glia*, 62(3), 374–386. <https://doi.org/10.1002/glia.22609>
- Mutsaers, S. E., & Carroll, W. M. (1998). Focal accumulation of intra-axonal mitochondria in demyelination of the cat optic nerve. *Acta Neuropathologica*, 96(2), 139–143. <https://doi.org/10.1007/s004010050873>



- Nave, K.-A., & Werner, H. B. (2014). Myelination of the nervous system: Mechanisms and functions. *Annual Review of Cell and Developmental Biology*, 30, 503–533. <https://doi.org/10.1146/annurev-cellbio-100913-013101>
- Ness, J. K., Mitchell, N. E., & Wood, T. L. (2002). IGF-I and NT-3 signaling pathways in developing oligodendrocytes: Differential regulation and activation of receptors and the downstream effector Akt. *Developmental Neuroscience*, 24(5), 437–445. <https://doi.org/10.1159/000069050>
- Pandit, A., Vadnal, J., Houston, S., Freeman, E., & McDonough, J. (2009). Impaired regulation of electron transport chain subunit genes by nuclear respiratory factor 2 in multiple sclerosis. *Journal of the Neurological Sciences*, 279(1–2), 14–20. <https://doi.org/10.1016/j.jns.2009.01.009>
- Prusky, G. T., Alam, N. M., Beekman, S., & Douglas, R. M. (2004). Rapid quantification of adult and developing mouse spatial vision using a virtual optomotor system. *Investigative Ophthalmology & Visual Science*, 45(12), 4611. <https://doi.org/10.1167/iovs.04-0541>
- Ray, A. K., DuBois, J. C., Gruber, R. C., Guzik, H. M., Gulino, M. E., Perumal, G., ... Shafit-Zagardo, B. (2017). Loss of Gas6 and Axl signaling results in extensive axonal damage, motor deficits, prolonged neuroinflammation, and less remyelination following cuprizone exposure. *Glia*, 65(12), 2051–2069. <https://doi.org/10.1002/glia.23214>
- Robinson, B. H. (2006). Lactic acidemia and mitochondrial disease. *Molecular Genetics and Metabolism*, 89(1–2), 3–13. <https://doi.org/10.1016/j.ymgme.2006.05.015>
- Romanelli, R. J., Mahajan, K. R., Fulmer, C. G., & Wood, T. L. (2009). Insulin-like growth factor-I-stimulated Akt phosphorylation and oligodendrocyte progenitor cell survival require cholesterol-enriched membranes. *Journal of Neuroscience Research*, 87(15), 3369–3377. <https://doi.org/10.1002/jnr.22099>
- Ruiz, M., Bégou, M., Launay, N., Ranea-Robles, P., Bianchi, P., López-Erauskín, J., ... Pujol, A. (2018). Oxidative stress and mitochondrial dynamics malfunction are linked in Pelizaeus-Merzbacher disease. *Brain Pathology*, 28(5), 611–630. <https://doi.org/10.1111/bpa.12571>
- Saab, A. S., Tzvetanova, I. D., & Nave, K. A. (2013). The role of myelin and oligodendrocytes in axonal energy metabolism. *Current Opinion in Neurobiology*, 23(6), 1065–1072. <https://doi.org/10.1016/j.conb.2013.09.008>
- Sanz-Rodríguez, M., Gruart, A., Escudero-Ramírez, J., de Castro, F., Delgado-García, J. M., Wandosell, F., & Cubelos, B. (2018). R-Ras1 and R-Ras2 are essential for oligodendrocyte differentiation and survival for correct myelination in the central nervous system. *The Journal of Neuroscience*, 38(22), 5096–5110. <https://doi.org/10.1523/JNEUROSCI.3364-17.2018>
- Sathornsumetee, S., McGavern, D. B., Ure, D. R., & Rodríguez, M. (2000). Quantitative ultrastructural analysis of a single spinal cord demyelinated lesion predicts total lesion load, axonal loss, and neurological dysfunction in a murine model of multiple sclerosis. *American Journal of Pathology*, 157(4), 1365–1376. [https://doi.org/10.1016/S0002-9440\(10\)64650-0](https://doi.org/10.1016/S0002-9440(10)64650-0)
- Savvaki, M., Panagiotaropoulos, T., Stamatakis, A., Sargiannidou, I., Karatzioula, P., Watanabe, K., ... Kleopa, K. A. (2008). Impairment of learning and memory in TAG-1 deficient mice associated with shorter CNS internodes and disrupted juxtaparanodes. *Molecular and Cellular Neuroscience*, 39(3), 478–490. <https://doi.org/10.1016/j.mcn.2008.07.025>
- Simons, M., & Nave, K. A. (2016). Oligodendrocytes: Myelination and axonal support. *Cold Spring Harbor Perspectives in Biology*, 8(1), 1–15. <https://doi.org/10.1101/cshperspect.a020479>
- Singh, G., Hashimoto, D., Yan, X., Helft, J., Park, P. J. Y., Ma, G., ... Chan, A. M. (2012). R-Ras is required for murine dendritic cell maturation and CD4 + T-cell priming. *Blood*, 119(7), 1693–1701. <https://doi.org/10.1182/blood-2011-05-357319>
- Snaidero, N., & Simons, M. (2017). The logistics of myelin biogenesis in the central nervous system. *Glia*, 65(7), 1021–1031. <https://doi.org/10.1002/glia.23116>
- Sock, E., & Wegner, M. (2019). Transcriptional control of myelination and remyelination. *Glia*, 67(11), 2153–2165. <https://doi.org/10.1002/glia.23636>
- Stys, P. (2005). White matter injury mechanisms. *Current Molecular Medicine*, 4(2), 113–130. <https://doi.org/10.2174/1566524043479220>
- Suter, U., & Scherer, S. S. (2003). Disease mechanisms in inherited neuropathies. *Nature Reviews Neuroscience*, 4(9), 714–726. <https://doi.org/10.1038/nrn1196>
- Thangavel, R., Sahu, S. K., van Hoesen, G. W., & Zaheer, A. (2009). Loss of nonphosphorylated neurofilament immunoreactivity in temporal cortical areas in Alzheimer's disease. *Neuroscience*, 160(2), 427–433. <https://doi.org/10.1016/j.neuroscience.2009.02.037>
- Timmler, S., & Simons, M. (2019). Grey matter myelination. *Glia*, 67(11), 2063–2070. <https://doi.org/10.1002/glia.23614>
- Trapp, B. D., & Stys, P. K. (2009). Virtual hypoxia and chronic necrosis of demyelinated axons in multiple sclerosis. *The Lancet Neurology*, 8(3), 280–291. [https://doi.org/10.1016/S1474-4422\(09\)70043-2](https://doi.org/10.1016/S1474-4422(09)70043-2)
- Tsutsui, S., & Stys, P. K. (2013). Metabolic injury to axons and myelin. *Experimental Neurology*, 246, 26–34. <https://doi.org/10.1016/j.expneurol.2012.04.016>
- Umino, Y., Solessio, E., & Barlow, R. B. (2008). Speed, spatial, and temporal tuning of rod and cone vision in mouse. *Journal of Neuroscience*, 28(1), 189–198. <https://doi.org/10.1523/JNEUROSCI.3551-07.2008>
- Waxman, S. G. (1998). Demyelinating diseases - new pathological insights, new therapeutic targets. *New England Journal of Medicine*, 338, 323–325.
- Witte, M. E., Lars, B., Rodenburg, R. J., Belien, J. A., Musters, R., Hazes, T., ... van Horsen, J. (2009). Enhanced number and activity of mitochondria in multiple sclerosis lesions. *Journal of Pathology*, 219, 193–204. <https://doi.org/10.1002/path.2582>
- Witte, M. E., Nijland, P. G., Drexhage, J. A. R., Gerritsen, W., Geerts, D., van het Hof, B., ... van Horsen, J. (2013). Reduced expression of PGC-1 $\alpha$  partly underlies mitochondrial changes and correlates with neuronal loss in multiple sclerosis cortex. *Acta Neuropathologica*, 125(2), 231–243. <https://doi.org/10.1007/s00401-012-1052-y>
- Yan, X., Yan, M., Guo, Y., Singh, G., Chen, Y., Yu, M., ... Chan, A. M. (2015). R-ras regulates murine T cell migration and intercellular adhesion molecule-1 binding. *PLoS One*, 10(12), 1–19. <https://doi.org/10.1371/journal.pone.0145218>
- Yan, X., Yang, F., Lukas, J., Witt, M., Wree, A., Rolfs, A., & Luo, J. (2014). Hyperactive glial cells contribute to axonal pathologies in the spinal cord of Npc1 mutant mice. *Glia*, 62(7), 1024–1040. <https://doi.org/10.1002/glia.22659>
- Youle, R. J., & van der Bliek, A. M. (2012). Mitochondrial fission, fusion, and stress. *Science*, 337(6098), 1062–1065. <https://doi.org/10.1126/science.1219855>
- Zamboni, J. L., Zhao, C., Ohno, N., Campbell, G. R., Engeham, S., Ziabreva, I., ... Mahad, D. J. (2011). Increased mitochondrial content in remyelinated axons: Implications for multiple sclerosis. *Brain*, 134(7), 1901–1913. <https://doi.org/10.1093/brain/awr110>

## SUPPORTING INFORMATION

Additional supporting information may be found online in the Supporting Information section at the end of this article.

**How to cite this article:** Alcover-Sanchez B, Garcia-Martin G, Escudero-Ramirez J, et al. Absence of R-Ras1 and R-Ras2 causes mitochondrial alterations that trigger axonal degeneration in a hypomyelinating disease model. *Glia*. 2021; 69:619–637. <https://doi.org/10.1002/glia.23917>